Title: MULTIPLE METAL SOURCES IN THE GLACIOMARINE FACIES OF THE NEOPROTEROZOIC JACADIGO IRON FORMATION IN THE "SANTA CRUZ DEPOSIT", CORUMBÁ, BRAZIL

Author: Thomas Angerer Steffen G. Hagemann Detlef Walde Galen P. Halverson Adrian J. Boyce

PII: S0301-9268(16)00011-5
DOI: http://dx.doi.org/doi:10.1016/j.precamres.2016.01.002
Reference: PRECAM 4421

To appear in: *Precambrian Research*

Received date: 18-5-2015
Revised date: 17-11-2015
Accepted date: 6-1-2016

Please cite this article as: Angerer, T., Hagemann, S.G., Walde, D., Halverson, G.P., Boyce, A.J.,<ce:small-caps>Multiple metal sources in the glaciomarine facies of the Neoproterozoic Jacadigo iron formation in the "Santa Cruz deposit", Corumbá, Brazil</ce:small-caps>, *Precambrian Research* (2016), http://dx.doi.org/10.1016/j.precamres.2016.01.002

Highlights

- The Banda Alta Member BIF precipitated in a redox-stratified seawater basin influenced by metal-enriched, anoxic seawater in the lower zone and diluted, oxic continental solutes from melting glaciers and rivers in the upper zone.
- Complex BIF stratigraphy with carbonate-rich and silica-rich facies and resedimented diamictites and hematite muds are a response to juxtaposing glacial advance/retraction cycle and glacial isostatic adjustment.
- Microbial activity facilitating calcium carbonate spheroids and mats and negative $\delta^{57}Fe$ values in BIF in relatively shallow water above a redoxcline.
- LREE/HREE fractionation, Ce_{PAAS}-anomaly, Y/Ho, base metals abundances, Zn/Co, as well as C and Fe isotopes are combined to distinguish following metal sources: (1) redox-stratified Neoproterozoic seawater, (2) metal-enriched fluids derived from altered crust, (3) oxidized continental solutes, and (4) terrigenous detritus.

Multiple metal sources in the glaciomarine facies of the Neoproterozoic Jacadigo iron formation in the "Santa Cruz deposit", Corumbá, Brazil

Thomas Angerer[1]*, Steffen G Hagemann[2], Detlef Walde[3], Galen P Halverson[4], Adrian J Boyce[5]

[1] Institute of Mineralogy and Petrography, University of Innsbruck, Austria

[2] Centre for Exploration Targeting, University of Western Australia (UWA), Perth, Australia

[3] Instituto de Geociências, Universidade de Brasília (UnB), Brasília, Brazil

[4] Department of Earth & Planetary Sciences, McGill University, Montreal, Quebec/Canada

[5] Scottish Universities Environmental Research Centre (SUERC), University of Glasgow, Great Britain

*corresponding author: thomas.angerer@uibk.ac.at (address: University of Innsbruck, Innrain 52f, 6020 Innsbruck, Austria)

Abstract

The Rapitan-type banded iron formation (BIF) in the Banda Alta Formation (Fm) of the Neoproterozoic Jacadigo Group in Brazil was deposited in a redox-stratified, marine sub-basin, which was strongly influenced by glacial advance/retraction cycles with temporary influx of continental freshwater and upwelling metal-enriched seawater from deeper anoxic parts. These new finding are based on new stratigraphic, whole-rock geochemical, and stable Fe and C isotope data from the "Santa Cruz" hematite deposit near Corumbá, Mato Grosso do Sul, where a

stratigraphy of lower and upper dolomite-rich and intermediate chert-rich BIF facies with up to three intercalated diamictites is revealed. The Ca-Mg-Fe-Mn-carbonate-chert and chert BIF (~30-45 wt% Fe) of the lower dolomite-rich facies shows chemical signatures consistent with well-oxidized seawater, i.e. low $(Pr/Yb)_{PAAS}$, strong negative Ce_{PAAS}-, and positive Gd_{PAAS}- and Y_{PAAS}-anomalies, as well as negative-$\delta^{13}C$ carbonate typical for Neoproterozoic glaciogenic carbonates. Sedimentation in a rather shallow water depth during relatively warm interglacial periods was likely influenced by abundant freshwater from fluviatile runoff and melting icebergs. In such conditions abundant microbial activity accommodated CO_2 sequestration in carbonates as spheroids and mats and fractionated $\delta^{57}Fe$ (-2.6 and -1.2‰) in primary Fe-hydroxides. In contrast, the intermediate chert-rich facies, characterized by chert-hematite BIF (~35-55 wt% Fe) and isolated hematite chert and hematite mud, recorded trace element signatures of non-oxidized (absence of Ce anomalies and variable Y_{PAAS}-anomalies), more metal-enriched (Fe, Mn, Si, Ni, Zn, Pb, U) seawater, thus deposition was within and below the shallow-level redoxcline during ice cover. Colder water and isolation from sunlight reduced microbial activity, and thus an almost non-fractionated $\delta^{57}Fe$ (-0.7 to 0.0‰) fluid signature reveals that hydrothermal (MOR) vents or (sub-) seafloor alteration of mafic or felsic rocks, or shales fertilized seawater with metals. All results lead to the model that the Jacadigo Group formed during one major marine transgression-regression cycle, and BIF facies in the Banda Alta Fm were a response to first- and second-order periodic variations of the depth of the redoxcline, induced by the juxtaposition of glacial advance/retraction cycles, active graben tectonics, and glacial isostatic adjustment or eustatic water level changes. The chert-rich BIF facies marked the maximum of transgression. Age and tectonic setting of the Jacadigo basin remains contentious: it

may represent a continental back arc basin of the Brasiliano collision zone (~590 Ma), in which submarine alteration was possibly related to low-temperature hydrothermal fluids moving through the active graben system (as an alternative to basin-wide benthic pore water flux). This would place the Jacadigo group to the suite of Ediacarian "Gaskier" glaciations, although a relationship to the Marinoan glaciation (660-635 Ma), mainly based on the published sedimentation age-bracket of 706-587 Ma, is also possible.

Keywords: Neoproterozoic glaciation; Jacadigo Group; Rapitan-type banded iron formation; rare earth elements; Fe isotopes

1. Introduction

1.1. BIF-hosted iron ore in the Neoproterozoic glaciogenic context

Banded and granular iron formation (BIF and GIF) are abundant in Archean to earliest Paleoproterozoic (volcano-) sedimentary successions. No significant iron formation occurs in the rock record between 1.8 Ga and 0.7 Ga, but BIF reappeared in many Neoproterozoic sedimentary successions, most of them associated with Sturtian (ca 715-680 Ma) and Marinoan (ca 660-635 Ma), and some with the Ediacarian (e.g., Gaskier: ~585-582 Ma: Bowring et al., 2003) glacial events (Hoffman et al., 2011). BIF are widely accepted as chemical proxies of the ancient marine hydrosphere, as these rocks recorded the seawater chemistry from which they were precipitated. Correspondingly, the association of those chemical sediments with Neoproterozoic glacial deposits provide critical evidence for Neoproterozoic syn- and post-

glaciation climate (Hoffman et al., 2011). Although the concurrent records of Neoproterozoic glaciogenic sediments is a central component of the snowball Earth model (Hoffman et al., 1998 and references therein), there is a recognition now that the Neoproterozoic BIF occurrence is a result of a culmination of controls, including metal-fertilization of local sub-basins (Cox et al., 2013). One of the most significant Neoproterozoic BIF occurs in the Jacadigo Group near Corumbá, Mato Grosso do Sul, Brazil, but nevertheless its depositional age and exact setting remain contentious (c.f., Walde and Hagemann, 2007). A simplified glaciomarine Fe and Mn ore model for the Morro do Urucum deposit proposed by Schneider (1984) and Schreck (1984) and later summarized by Urban et al. (1992) is widely accepted. Klein and Ladeira (2004) subsequently supported this model with trace geochemical and carbon isotope data from the same locality. A non-glaciogenic deposition model has been proposed by Freitas et al. (2011). The "Santa Cruz deposit" at the eastern edge of the Urucum inselberg massif (Figure 1), currently owned by Vetria Mineração, is a well-developed exploration project in terms of map and core availability. It represents a perfect natural laboratory to investigate the controversial BIF deposition. Here we present new field observations including detailed diamond core logs, petrographical, geochemical, and Fe and C isotope data. Based on this new data we propose a chemostratigraphic model for the local BIF facies.

1.2. **Geology of the Corumbá region**

The Corumbá region is located on the eastern edge of the Amazon craton-Rio Apa block, about 20-30 km west of its tectonic contact with the Brasiliano Paraguay belt (Figure 1a). In this region, two sets of extensional structures are identified: the poorly exposed eastern extremity of the WNW-ESE-trending, 500 km long, Chiquitos-Tucavaca aulacogen (a failed rift arm) and the

NE-SW-trending, 10-20 km long, Corumbá graben system (Jones, 1985). In the Corumbá area, two lithostratigraphic groups have been distinguished: the Jacadigo and Corumbá Groups (de Almeida, 1945; Dorr II, 1945). A stratigraphic correlation of the Jacadigo with the Boqui Group in Bolivia (Figure 1b) has been established (Graf Jr et al., 1994). According to Dorr II (1945) the Jacadigo Group consists of three formations, the Urucum, the Córrego das Pedras, and the Banda Alta Fms. The Urucum Fm consists of coarse arkoses and conglomeratic sandstones and unconformably overlies the basement of the Amazon craton-Rio Apa block. The Córrego das Pedras Fm consists of variable siliciclastic rocks and hosts a basal manganese ore layer. The Banda Alta Fm is made up of hematite-rich BIF with intercalated sandstones, arkoses, diamictites, and manganese ore. In the Banda Alta Fm, dropstones have been identified in BIF and Barbosa (1949) suggested a glaciogenic origin of these rock features. In the alternative lithostratigraphy of de Almeida (1945), rocks of the intermediate Córrego das Pedras Fm are subsumed into the Urucum Fm, and the Banda Alta Fm equals the Santa Cruz Fm (hence the given name of the hematite deposits). In the present publication the subdivision of Dorr II (1945) is used, mainly to avoid any confusion regarding the use of "Santa Cruz". The Corumbá Group, unconformably overlying the truncated Banda Alta Fm, is made up of dolostones in the lower Bocaina Fm, and limestones in the upper Tamengo Fm. The Tamengo Fm contains an Ediacara-like fauna (Walde et al., 2015, and references therein).

Unequivocal depositional ages, and therefore evidences for a correlation with globally occurring ice ages, are not available for the Jacadigo Group. Basement granites have igneous K/Ar age of ca. 889 ± 44 Ma (Hasui and Almeida, 1970), providing a maximum age for overlying sedimentary rocks. The Banda Alta Fm BIF has been interpreted as largely coeval to the glaciomarine diamictites of the Puga Formation to the South, which has a maximum age (based

126 on detrital zircons) of 706 ± 9 Ma (Babinski et al., 2013). In Bolivia, the Pimienta Fm, which is
127 possibly a lower part of the Boqui Group (therefore potentially correlative with the Jacadigo
128 Group), consists of tuffs, agglomerates, lapilli, and volcanic breccias of basaltic composition
129 (O'Connor and Walde, 1985; Litherland et al., 1986). Associated plutonic rocks have a lower
130 Ediacarian K/Ar age of 623 ± 15 Ma (Walde, 1988). However, inclusion of the Pimienta Fm in
131 the Jacadigo Group remains hypothetical. A minimum age for the Jacadigo Group of 587 ± 7 Ma
132 was recently obtained by $^{40}Ar/^{40}Ar$ dating of diagenetic cryptomelane in the Mn-formation at
133 Morro do Urucum (Piacentini et al., 2013). Based on stratigraphical, sedimentological and
134 structural data, Trompette et al. (1998) suggested the following evolution for the Neoproterozoic
135 sequences in the Corumbá region: During the late Cryogenian or early Ediacarian (ca 600-570
136 Ma), extensional tectonics generated a system of grabens parallel to the border of the Amazon
137 craton. This extensional event was probably synchronous with early stages of the Brasiliano
138 collision, which has been dated at ~590 Ma (Pimentel and Fuck, 1992; Pimentel et al., 1996).
139 This relationship and timing suggest a sedimentation during the Ediacaran period, and assuming
140 that the diagenetic-metamorphic sequence commenced shortly (ca. <10 Ma) after deposition, the
141 published minimum depositional age of 587 ± 7 Ma (Piacentini et al., 2013) agrees with this. A
142 deposition of the Jacadigo Group associated with the Marinoan glaciation lacks unequivocal,
143 direct geochronological evidences, too, but is suggested by the 623 ± 15 Ma age of the Pimienta
144 Fm, considering a correlation with the Boqui Group. Even a Sturtian age cannot be ruled out
145 based on the hypothetical correlation with the Puga Fm, as proposed by Hoffman and Li (2009).
146 For comparison, the Rapitan IF in the Mackenzie Mountains, northwest Canada, is with its 716.5
147 ± 0.2 Ma age (U/Pb zircon date: Macdonald et al., 2010) a Sturtian deposit.

Transgression of glacioeustatic origin initiated the deposition of dolostones of the Corumbá Group during the Ediacarian age (Trompette et al., 1998). Weak NNW-SSE trending folds, probably synchronous with deformation and metamorphism in the Paraguay belt (545-500 Ma), affected the Jacadigo and Corumbá Groups (D'el-Rey Silva et al., in press). Finally, Pliocene (ca 3 Ma) tectonic inversion of the graben system and development of the present inselberg topography (the Urucum massif) are correlated to the subsidence of the basement and formation of the Pantanal basin (Ussami et al., 1999). The flat to shallowly south-easterly dipping BIF in the "Santa Cruz deposit" represents the south-easternmost extension of the Urucum inselberg massif (Figure 2a).

2. Geological setting of the "Santa Cruz deposit"

2.1. **Stratigraphic column**

Based on mapping and core logging a generalised stratigraphic profile of the "Santa Cruz deposit" was constructed (Figure 3). Siliciclastic units of the Urucum Fm, the Córrego das Pedras Fm, or diamictite of the Banda Alta Fm, all sensu Dorr II (1945), rest unconformably above a gneissic basement high of the Rio Apa Block. The Urucum Fm is characterised by grey-green, fine to medium-coarse-grained siliciclastic rocks with calcitic cement, locally displaying cross-bedding and inverse grading characteristic of a fluvial environment. Minor chert-siderite-magnetite-hematite BIF is present in the Urucum Fm. The Córrego das Pedras Fm is defined by sandstones, arcoses, micro-conglomerates, and up to three layers (each <2m) massive Mn-oxide or Mn-rich arcoses (cryptomelane-braunite-dominated: Piacentini et al., 2013). The sequence

with four well defined Mn-rich horizons described at Morro do Urucum (Dorr II, 1945) and being mined is not encountered in the "Santa Cruz deposit".

The Banda Alta Fm hosts dolomite-chert-hematite BIF in a *lower and upper carbonaceous zone*, and jaspilitic chert-hematite BIF in an *intermediate siliceous zone*. BIF with clastic layers are subordinately dispersed in the column. Diamictite units are discontinuously intercalated in BIF and have thicknesses up to a few decametres. The upper diamictite and its dolomite-rich BIF footwall are the highest preserved units of the Banda Alta Fm in the deposit and is located only in eastern portion of the deposit (see e.g., STCR-DD-28-24 and STCR-DD-26-22 in Figure 4a, and STCR-DD-68-24 in Figure 4b). The uppermost sequence of the Banda Alta Fm is completely eroded in the region. Despite local evidence of compression (see following section), no significant tectonic duplication of the stratigraphy is observed in the deposit, allowing a thickness estimating of the Banda Alta Fm BIF to be 360 metres. This is compatible to Morro do Urucum (>300 metres according to Dorr II, 1945).

The lower, discontinuously developed, reddish ferruginized diamictite has a hematite-calcitic cement-matrix. The ferruginized middle diamictite, with a hematite-silicate cement-matrix, is a well-developed marker horizon throughout the deposit (see marker lines in Figure 4). The largely non-ferruginized upper diamictite has a silt-calcite-chlorite cement-matrix, local ferruginization is present close to intraformational cherts and footwall BIF. Its lateral continuation is unclear due to erosion.

The middle diamictite is stratigraphically enveloped by typical footwall and hanging wall facies: a hematite rock ("hematite mud") forms the immediate one to two metres below the diamictite, and a hematite chert (or "hematite silt"?) is developed in the hanging wall, commonly as a decimetre to metre thick unit. The footwall hematite mud shows both, laminated or massive-

brecciated texture; the latter being rich in randomly oriented chert-mesoband fragments and a featureless hematite matrix. Such a reworked breccia facies suggests a high-energy deposition of overlying diamictite flows, whereas the laminated type indicates less impact of the diamictite flow. The hanging wall hematite chert is intercalated with BIF and therefore represents a transition from diamict clastic environment to chemical sedimentation of the hanging wall jaspilitic BIF. Locally, decimetre to metre thick units of hematite chert and muds are intercalated and interfingered within the BIF. Hematite chert is limited to intermediate siliceous zone, whereas hematite muds also has carbonate components when located within the lower and upper carbonaceous zone.

2.2. **Deformation sequence**

In the region of the "Santa Cruz deposit", the Neoproterozoic rocks of the Jacadigo Group are deformed by a set of tectonic structures (D1, D2, D3, and D4: D'el-Rey Silva et al., in press). An early D_{x-1} is recorded as extentional graben structures associated with the opening of the Chiquitos-Tucavaca aulacogen parallel to the border of the Amazon craton with the Rio Apa block (Trompette et al., 1998). According to these authors, sedimentation of the Urucum Fm, and probably also the Banda Alta Fm, were coeval with the active graben teconics, leading to variable stratigraphic thicknesses throughout the depsoitional basin (Trompette et al., 1998). The D_1 is related to the diagenetic to very-low grade metamorphic burial. The D_{1a} is represented in BIF by ptygmatic crenulated, chert veinslets. A D_{1b}-foliation (S_{1b}) is ubiquitously present in siliciclastic rocks as a pervasively developed foliation and in BIF by shape prefered orientation of hematite and oblate flattened clastic and diagenetic nodules. The D_2 to D_3 events are associated with the tectonic evolution of the Paraguay and Tucavaca tectonic belts bordering the

Amazon Craton. The D_2 brittle-ductile deformation event led to the local thrusting of the Urucum over the Banda Alta Fm. Parts of the thrust slice is preserved in the eastern section of the deposit and is characterized by highly asymmetric, tight to isoclinal, F_2 folds (D'el-Rey Silva et al., in press). The D_3 open folding event comprises crustal shortening phases related to the Paraguay tectonic belt (NW-SE) and the closure of the Tucavaca failed rift basin (SW-NE) (D'el-Rey Silva et al., in press). The D_4 event is interpreted as the result of Pliocene (at ca. 3 Ma) block tectonics (c.f., Shiraiwa, 1994).

3. Sample selection and analytical methods

Drill core logging and grab sampling from drill core and outcrop was carried out by the authors during field work in 2013. Sampling was limited to unweathered BIF (avoiding those with clastic bands), hematite "mud", and hematite chert in the lower and intermediate zone, focusing on the facies transition from carbonaceous to siliceous BIF and investigating the role of chert- and hematite-rich endmember facies. Each analytical method (whole-rock geochemistry, Fe and C isotopes) was applied to a specific sample subset where the comparability between samples representing a specific lithology and stratigraphic position is given. Table 1 provides a list of samples and methods used and Figure 5 shows the sample locations.

3.1. **Whole-rock geochemical analyses**

The grab sampling strategy for the analyses of major elements, trace and rare earth elements (based on 0.5 to 0.8 kg aliquots) targeted specific lithologies, which are represented by eleven samples: five banded and podded chert-hematite BIF (CaO < 2.1 wt%), three banded and podded dolomite-chert-hematite BIF, two hematite muds, and one hematite chert (Table 1). Analyses

234 were performed by ActLabs Pacific Pty. Ltd. facility in Ancester, Canada. Samples were
235 crushed, split into fractions using a rifle splitter, and then pulverized in a mild carbon steel mill
236 (95% passing at 75 μm). Contamination during carbon mild steel pulverization is minor (<0.2%
237 Fe, traces of C, Mn, Si, Cr, Co). Cross-contamination between samples was minimized by
238 repeated silica washes. Sixty elements were analyzed by a combination of digestion and
239 analytical methods in order to determine the geochemical abundance using the most appropriate
240 method for each element or groups of elements. Loss of ignition (LOI) was determined at
241 1000°C. ActLabs incudes certified reference materials and duplicates into the analyzed batch for
242 quality control. Additionally, pre-milled certified reference material, BIF standard FER-3
243 (Alexander and Bau, 2009), was submitted together with the sample suites. The accuracy and
244 precision of ActLabs Pacific Pty. Ltd. is monitored since several years using this standard, and
245 monitoring data can be obtained from the first author. Data and calculated indices are provided in
246 Table 2.

247 3.2. **Fe isotopes in hematite**

248 Five hematite samples from selected lithologies were analyzed for stable Fe isotopes at McGill
249 University, Canada. Parts of nodule-free hematite bands from BIF samples were isolated using a
250 saw, then pulverized, and then treated for 0.5 hours in a warm 20% diluted HCL bath to dissolve
251 any minor dolomite (~<5 wt%). Various studies have indicated that no discernible fractionation
252 of iron phases is associated with acid treatment (Skulan et al., 2002; Beard and Johnson, 2004;
253 Severmann et al., 2006). Samples were analyzed at Geotop/UQAM in Montreal, Canada,
254 according to the methods used in Halverson et al. (2011). Approximately 10 mg of pulverized
255 samples were weighed into a Savillex Teflon beaker and dissolved for 24 hours at 80 °C in a 2

mL mixture of double-distilled 6 M HCl and concentrated HNO_3 and HF. The samples were then evaporated to dryness with excess HNO_3, then redissolved in 2.0 mL of 2 M HCl. Samples were again dried and then taken up in 0.5 mL of 6 M HCl for ion exchange chromatograpy. Fe was separated using Bio Rad AG1 X4, 200–400 mesh resin loaded into custom Teflon columns and separated from the matrix using 6 M HCl. Purified iron was eluted from the columns in 2 M HCl, which was then dried down and taken up in 0.5 M HNO_3. Solutions were analyzed in the Geotop Radiogenic isotope laboratory at the Université de Québec à Montréal on a Nu Instruments Nu Plasma II in in high-resolution mode via wet sample introduction. Instrumental mass bias was corrected by using the standard-sample-standard protocol, whereby delta values are calculated for each individual sample analyses against the average of standards before and after. Samples were analyzed three times each, yielding typical 1-sigma errors of <0.1 for $\delta^{57}Fe$ and <0.05 for $\delta^{56}Fe$. The data are reported in standard delta notation (per mil units) relative to the IRMM-14 reference standard.

3.3. **C isotopes in carbonate**

Six carbonate mineral separates from dolomite-rich BIF were analyzed for stable C isotopes at SUERC (Scottish Universities Environmental Research Centre), University of Glasgow. Samples were analyzed at SUERC (Scottish Universities Environmental Research Centre), University of Glasgow, on an Analytical Precision AP2003 mass spectrometer equipped with a separate acid injector system, after reaction with 105% H_3PO_4 under a He atmosphere at 70 °C. Isotopic results are reported using the conventional δ‰-notation. Mean analytical reproducibility based on replicates of the SUERC laboratory standard MAB-2 (Carrara Marble) was around ±0.2‰ for both carbon and oxygen. The $\delta^{13}C$ are reported relative to V-PDB.

4. Petrography

4.1. Dolomite-chert-hematite BIF and chert-hematite BIF

Dolomite-chert-hematite BIF in the lower and upper carbonaceous zone consists of hematite layers and carbonate-chert layers, which are locally weakly podded or rich in nodules (Figure 6a, b). Typically, gangue microbands are <0.5cm thin and mesobands 0.5 to ~5 cm thick and consist of fine to granoblastic, white to yellow dolomite-chert matrix and mm to sub-cm dolomite "intra-band" nodules (Figure 6a). So-called "inter-band" textures forming nodular iron formation, as shown in Figure 6b, are less common. It is likely that this pseudonodular texture formed by viscose mobility of the non-mixing components iron hydroxides and carbonate-chert mix, probably under pressure-induced thixotropic behavior during early diagenesis (c.f., Owen, 2003). Dolomite and chert may form distinct bands (Figure 6c, here folded at the microscale) and nodules (Figure 6d), or are interlocked forming mixed carbonate-chert matrices (Figure 6e). In these matrices, dolomite shows subhedral rhombic or granoblastic textures that partially overgrow chert (Figure 6e), thus dolomite and chert are texturally not in equilibrium. This suggests post-sedimentary *in-situ* growth (ripening?) of carbonate crystals and may be related to a diagenetic dolomitization event (see section 10.2 for discussion). Routine mineral staining and SEM mineral chemistry (*authors' unpublished data*) show variable Mn-Fe-content in all dolomite and minor Mn-calcite associated with dolomite.Collected dolomite-chert-hematite BIF samples are limited to unweathered banded and podded textures. This is to obtain a most-pristine BIF sedimentation-record in BIF samples across the transition from the lower carbonate- to intermediated chert-facies zone.

Jaspilitic chert-hematite BIF is commonly podded and only locally shows well-banded textures (Figure 7a, b). Chert-rich BIF show far less nodules in the gangue layers than the dolomite-chert-hematite BIF. The gangue matrix is a fine-grained, red cryptocrystalline hematite-impregnated chert (Figure 7c). The typical podding texture in unweathered chert-rich BIF is a result of removal of gangue ("dissolution-podding"), which is identified by dissolution seams parallel to bedding tracing the former mesoband (Figure 7b). Podded textures are less well-developed in the dolomite-hematite BIF of the lowermost Banda Alta Fm.

Hematite mesobands in all BIF are commonly a fine mix of anhedral hematite to microplaty hematite and minor gangue, i.e., chert or dolomite, or dolomite-chert (Figure 7d). The hematite grain sizes are commonly less than 20 μm, however single grains are fused to anhedral-massive or cellular aggregates (Figure 7e), giving the macroscopic metallic lustre to the hematite mesobands. Also, the microplaty hematite-rich textures may show lepidoblastic orientation of crystal shapes parallel to bedding (Figure 6f). This compaction fabric was generated by hematite re-orientation and/or growth most likely during late diagenesis. Dolomite and chert nodules are variously hematite-altered showing red, dusty, cryptocrystalline hematite or dense aggregates of finely intergrown microcrystalline hematite with metallic lustre.

Common, but heterogeneously distributed in gangue mesobands of all Banda Alta Fm BIF types, are microscopic spheroids up to 400 μm diameter (Figure 7e). These spheroids consist of secondary, concentric and/or radial symmetric, chert or dolomite, and are locally hematite-stained (Figure 7f).

4.2. **Hematite chert and mud**

The hematite chert is a banded-laminated to nodular-laminated type rock, characterized by less than 0.5 cm thick jaspilitic chert laminae alternating with thin hematite-rich laminae (<mm) (Figure 8a). Few isolated clast-like hematite grains suggest some influence of (hematitic?) detritus (Figure 8b). Hematite in the chert is commonly present as 10-20 µm small, chert-inclusion-rich, globular grains, and locally they form randomly oriented chains (or "needles") or aggregates (Figure 8c). Such hematite-"needles" may represent hematite-replaced fibrous silicates, which are typical for diagenetic to low-metamorphic Archean and Paleoproterozoic BIF (Klein, 1974; Klein, 2005). Hematite grains may also form layers of larger anhedral aggregates (Figure 8d).

Hematite muds are laminated or massive rocks with up to ~66 wt% Fe. There is a near absence of dolomite-chert gangue layers, only local chert lenses are observed (Figure 8e). The laminated texture is defined by alternating, bedding-parallel, hematite laminae of variable grain sizes and shapes. Three distinct hematite mud types are delineated: (1) reworked hematite mud (sample H-01): this mud is present just below the middle diamictite, as the hematite-rich endmember of breccia-muds that commonly contain fractures of chert layers. The texture in sample H-01 resembles a clastic texture of fused hematite grains that are oriented parallel to the bedding (Figure 8f). In some bands, hematite is completely fused leaving only relics of hematite clasts (Figure 8g). The overall clastic texture of this hematite mud type and the association with breccias provides evidence for a reworked nature. (2) chemical mud sediment (C-18): This mud is characterized by granoblastic hematite texture with distinct layers of variable grain sizes (Figure 8h). Textures do not provide evidence for clastic nature and the mud was probably

chemically precipitated, as the Fe-rich endmember of BIF. This is supported by the stratigraphic association with BIF. (3) leached-type hematite rock (not sampled): A completely different type of hematite rock is the leached type. The leached-type hematite rocks can be identified by dissolution seams at the edges of remnant gangue lenses and between hematite laminae. This lithology was generated by secondary, probably hypogene and supergene, silica or carbonate loss. The rock type is not part of the present investigation.

5. Major element geochemistry

5.1. **Dolomite-chert-hematite BIF and chert-hematite BIF**

Chert-hematite BIF (with CaO <2.1 wt%) show Fe contents of 45 to 56 wt% and define a negative linear correlation with SiO_2 (Figure 9a). Dolomite-chert-hematite BIF have on average lower Fe, Si, and Al contents compared to chert-hematite BIF, whereas Ca, Mg, and LOI are significantly enriched due to the abundance of dolomite (Figure 9b, c; for LOI see Table 2). All BIF samples have very low Al and Ti concentrations (Al_2O_3 <0.25 wt %, TiO_2 <0.031 wt%) and a positive correlation of both elements suggest that both derive from minor detrital components (Figure 10a). The limited number of samples suggests that podded BIF have higher Fe contents. Dissolution-podding of chert-hematite BIF is, therefore, associated with Fe upgrade from about ~35 wt% to up to 55 wt% in the unweathered section of the deposit.

The P_2O_5 content in dolomite-chert-hematite BIF is high with 0.36 to 0.38 wt% and low in chert-hematite BIF (<0.2 wt%). This corresponds to apatite abundances in the rocks (not shown in the petrography section). The dolomite-chert-hematite BIF have CaO/MgO ratios of 2.3 to 3.2, whereas the chert-hematite BIF have higher ratios of 3.0 to 9.0. Overall mean value is ~4.0,

362 which is much higher than in pure dolomite (1.4) and a result of Fe- and Mn-bearing dolomite,
363 and Mn-calcite, and apatite abundance.

364 5.2. **Hematite chert and mud**

365 The hematite chert sample H-03 is significantly depleted in Fe compared to other samples
366 (Figure 9a, Table 2). Consistent with the silica-dominated mineralogy, dolomite and apatite
367 related elements CaO, MnO, MgO, P_2O_5, and LOI are lowest in the sample set. Also, terrigenous
368 Al and Ti are very low and thus, despite its stratigraphic position overlying the clastic middle
369 diamictite, a dominantly chemical nature is suggested.
370 The two analyzed hematite mud samples have Fe grades of 58.7 and 66.3 wt% (Figure 9a, Table
371 2). In the slightly lower Fe grade sample H-01, the sum of MnO, MgO, CaO, P_2O_5, LOI is 0.55
372 wt%, whereas in contrast, the higher Fe grade sample C-18 shows a sum of 1.7 wt%. This
373 elemental pattern is consistent with the association of the samples with dolomite-chert-hematite
374 BIF (sample C-18) and chert-hematite BIF near the middle diamictite (sample H-01). However,
375 whole-rock geochemistry is not indicative for the genesis of the two distinct samples (i.e.,
376 reworked clastic mud and chemical precipitated mud).

377 6. REE and trace metal geochemistry

378 6.1. **Two distinct signature in BIF (REE I and II)**

379 The BIF samples and hematite mud sample C-18 reveal two distinct Post Archean Australian
380 Shale (PAAS)-normalized REE fractionation patterns (referred to REE I and REE II). The REE
381 I, represented by dolomite-chert-hematite (samples C-04, C-05, C-07) and podded chert-hematite
382 BIF (samples C-15, C-16, C-17), shows depletion towards LREE, quantified by $(Pr/Yb)_{PAAS}$,

383 $(Pr/Sm)_{PAAS}$, and $(Tb/Yb)_{PAAS} < 1$ (Table 2), and consistent negative Ce_{PAAS}- and positive
384 Gd_{PAAS}- and Y_{PAAS}-anomalies. These characteristics are consistent with modern seawater (Figure
385 11**Error! Reference source not found.**a). The chert-(dolomite)-hematite BIF samples C-01 and
386 C-14, as well as the hematite mud sample reveal a distinct pattern REE II, which is characterized
387 by stronger LREE depletion and near absence of the Ce_{PAAS}-anomaly (Figure 11**Error!**
388 **Reference source not found.**b). The REE I and II patterns have very similar HREE and Y
389 concentrations and define a mixing array in the $(Ce/Ce^*)_{PAAS}$ and $(Pr/Yb)_{PAAS}$ space (Figure
390 12a), suggesting a genetic relationship amongst both. Base metal concentrations are higher in
391 REE II than in REE I samples (Cu+Pb+Zn > 15 ppm and < 12 ppm, respectively, and Figure 12b
392 for Cu and Pb). This appears also to be the case for U (REE I <0.14 and REE II >0.16: Table 2),
393 albeit the fact that U depends on SiO_2, thus is generally higher in chert-rich BIF. An
394 "undisturbed" Mn to Co correlation is indicated for REE I samples, consistent with common Co
395 uptake by Mn-oxides (Figure 12c). However, significant deviation (elevated Co) is shown in
396 REE II samples pointing to more complex Co-hosts.
397 There are similarities, but also significant differences, between BIF from the "Santa Cruz
398 deposit" and contemporaneous Morro do Urucum deposit (Klein and Ladeira, 2004). Most
399 terrigenous elements Al, Ti (Figure 10a), as well as Zr (Figure 10d), base metals, and Rb (Figure
400 12d) are higher concentrated in BIF from Morro do Urucum. Nevertheless, the REE patterns
401 mostly resemble those from the Morro do Urucum BIF (compare Figure 11a, b, with d**Error!**
402 **Reference source not found.**), with the exception of the more pronounced Ce-anomalies in REE
403 I BIF. BIF from the Rapitan IF (Halverson et al., 2011; Baldwin et al., 2012) resembles the REE
404 II geochemistry, which the exception of their generally lower Y/Ho ratio (Figure 12e).

6.2. **Comparable signature in hematite mud and chert (REE III)**

A third distinct REE pattern (REE III), represented by the reworked hematite mud (H-01) and hematite chert (H-03), is characterized by a wavy, but rather flat (shale-like), fractionation pattern, an insignificant Ce_{PAAS}-anomaly, and a weak *negative* Y_{PAAS}-anomaly. This heterogeneous REE pattern does not resemble the signatures in other BIF types and thus indicate largely contrasting metal sources. Hematite chert is significantly enriched in Zr and Cu (Figure 10d, Figure 12b), whereas Ti, Al, Co and Ni (Figure 10a, Figure 12c, Table 2) are depleted. The REE-abundance and fractionation pattern of REE III samples are strikingly similar to "hematitic muds and silts" in the Rapitan IF (Figure 11c, Figure 12a**Error! Reference source not found.**) reported by Halverson et al. (2011). Just minor differences are the HREE fractionation pattern and slightly higher Y/Ho in the Rapitan muds and silts (Figure 12e). Accessory detrital illite, feldspar, and chlorite are present in those rocks (Halverson et al., 2011), and, although not observed in the REE III samples, they may be represented by the abundant hematite-replaced silicates.

6.3. **Detritus and possible effects on trace element chemistry**

Using REE pattern as proxies of chemical seawater conditions have to be discussed in light of potential diluting effect of detritus. The low $(Pr/Yb)_{PAAS}$ and high Y/Ho ratios (i.e., super-chondritic, >26.22: Pack et al. (2007)) in REE I and REE II are far from unity (i.e., not shale-like). The lack of covariance between REE indices and Ti and Al supports that the influence of terrestrial-derived material on the reported REE fractionation indices is negligible (Figure 10b, c). Diagrams of $(Pr/Yb)_{PAAS}$ and Y/Ho versus Ti (not shown) also lack such covariance. Within the REE I and II types there is no covariance of the Y/Ho anomaly with Zr (Figure 10d) and Al.

Therefore, contribution of detrital sources in REE I and II is considered insignificant with respect to the potential obliteration of a pristine seawater signature.

In the absence of terrigenous detritus, important REE hosts are Ca-carbonates and apatite (predominantly LREE and MREE based on similarity of ionic radii: Shannon (1976) and hematite (predominantly HREE with smaller ionic radii). This is supported by a weak covariance of Pr with CaO and P_2O_5 concentration, whereas no significant covariance of Pr with other elements is detected. Dolomite-apatite content significantly shape LREE fractionation within REE I (higher $(Pr/Yb)_{PAAS}$ ratios and lower $(Ce/Ce^*)_{PAAS}$) (Figure 10e, Figure 11a) but the key trace element characteristics to differentiate REE I and REE II are independent on dolomite-apatite content. This allows the conclusion that REE I and REE II types BIF recorded seawater signatures, co-precipitated dolomite-apatite have only minor impact on trace element geochemistry and their primary phases were most likely seawater-derived (based on the similarity of REE pattern compared with dolomite-free BIF). The actual genesis of the present carbonate mineralogy, however, is likely secondary diagenetic and will be discussed in section 10.2.

In light of the very low terrigenous detrital components Al and Ti in hematite chert (Figure 10a), its REE pattern is consistent with volcanogenic ash origin (Pearce et al., 2013; Tepe and Bau, 2014) or indicate a certain fluid signature. The hematite-pseudomorphs (Figure 8c) may be an alteration product after volcanogenic Al-free Fe-silicates such as greenalite, stilpnomelane, minnesotaite, or riebeckite. However, the hematite mud sample H-01 lacks high Zr concentrations despite showing an almost equivalent REE III pattern. On the other hand, there is a striking similarity of REE III with those of modern low-temperature (~30 °C) submarine vent fluids reported by Michard et al. (1993), as shown in Figure 11c). Conclusively, the wavy REE

III pattern clearly suggests a component mix, likely including volcanic ash and/or terrigenous detritus, but potentially it indicates low-temperature hydrothermally fertilized seawater. The origin remains contentious and will be discussed in a speculative way.

6.4. **Post-sedimentary alteration and possible effects on trace element chemistry**

The sample selection was rigorous in terms of avoiding weathering artefact (such as clay and goethite) which may modify geochemical signatures. However, post-depositional, (cryptic) hydrothermal alteration was impossible to avoid and therefore alteration is an alternative explanation for the distinct base metals, Pb, U, and LREE patterns in unweathered BIF. Petrographical evidence for diagenetic alteration do exists: silica veinlets, dolomite recrystallization, hematite replacement, with the most noticeable being hypogene gangue leaching and hematite upgrade by dissolution-podding. Cr (and V) shows a positive covariance with Fe content (Figure 12f), and as these metals are partitioned into the hematite lattice (c.f., Nadoll et al., 2014; Hensler et al., 2015), their covariance is a direct result of podding. All other geochemical signatures in BIF, e.g., Al, Ti, REE fractionation and anomalies, are independent from dissolution-podding, and therefore this alteration is not significant in terms of primary fluid signatures.

Minor LREE mobility in dolomite-chert-hematite BIF, e.g., by carbonate recrystallization, is suggested by the variation of La to Gd abundances amongst dolomite-chert-hematite BIF samples (Figure 11**Error! Reference source not found.**a). However, REE budget in modern and Devonian microbial reef-calcite (Figure 11**Error! Reference source not found.**a) show that carbonates can show minor variation in LREE fractionation compared to the seawater they were

471 precipitated from. In any case, this LREE variation is insignificant in terms of the general REE
472 pattern.
473 Hydrothermal alteration of banded chert-hematite BIF (REE II) to podded BIF (REE I) is an
474 alternative explanation for the chemical variance and would involve a depletion of base metals,
475 Pb and U, and an addition of LREE by Ce-HREE-depleted apatite or monazite, causing the
476 negative Ce_{PAAS}-anomaly. However, whereas the hydrogenetic Co-Mn correlation appears
477 "pristine" in REE I BIF (Figure 12c), there is deviation from this trend in REE II BIF. This
478 suggests that, if at all, only REE II samples enjoyed limited hydrothermal alteration involving
479 mobility of Co and Mn.
480 In conclusion, based on the REE patterns in the present sample set, the effects of post-
481 depositional alteration or chemical exchange in whole-rock chemistry are considered as not
482 significant. However, effects at the micro-scale remain contentious and need to be explored in
483 more detail with, for example, stable oxygen isotopes and element mapping.

484 ## 7. Fe isotopes in hematite

485 The subset of five samples are petrographically representative for BIF and hematite mud
486 lithologies of the lower carbonaceous (samples C-06 and C-11) and intermediate siliceous
487 (samples C-14, H-14, and H-15) zone and correspond to geochemical samples as shown in Table
488 1. The Fe isotope data (expressed in per mil units relative to the IRMM-14 standard) show
489 negative $\delta^{57}Fe$ values for BIF (Table 3). Values are low in the dolomite-rich hematite BIF (-2.6
490 and -1.2 ‰), higher in the chert-hematite BIF (-0.7 ‰) and highest in the associated reworked
491 hematite mud (-0.3 and 0.0 ‰). The 1σ range from 0.01 to 0.07 indicates that the data ranges of
492 each group (albeit limited in number) are distinct. This allows a general assessment of a

493 lithologically controlled iron isotope fractionation, with dolomite-rich BIF being most depleted
494 in $\delta^{57}Fe$ and hematite mud least. The effect of sedimentological reworking in the hematite mud
495 on the iron isotopic signatures is considered to be minor. For comparison, Fe isotopes in the
496 Rapitan IF record $\delta^{57}Fe$ values of -0.67 to +1.2 ‰, with an up-stratigraphic increase (Table 3).

497 8. C isotopes in dolomite

498 The selected samples are petrographically representative for dolomite-chert-hematite BIF
499 lithologies of the lower carbonaceous zone. In the "Santa Cruz deposits" (this study) and Morro
500 do Urucum deposits (Klein and Ladeira, 2004), carbonates show negative $\delta^{13}C_{CARB}$ values
501 (CARB means carbonate-hosted carbon) relative to seawater, with a total range of -3.4 to -7.0 ‰
502 PDB (Table 4). At the "Santa Cruz deposit" the range of $\delta^{13}C_{CARB}$ values in selected samples is
503 limited to -3.4 to -4.3 ‰ PDB. In comparison, carbonates in the Rapitan IF recorded less
504 depletion in $^{13}C_{CARB}$ with values between -0.67 to -3.37 ‰ (Klein and Beukes, 1993).

505 9. Fluid source signatures

506 9.1. Redox-stratified seawater and influx of continental solutes

507 The REE I and REE II patterns are mostly consistent with Phanerozoic (modern) seawater (Bau
508 et al., 1995; Alibo and Nozaki, 1999; Bau and Dulski, 1999) as sown in Figure 11a**Error!**
509 **Reference source not found.**. Seawater-typical positive La_{PAAS} anomalies are probably masked
510 by the strong Ce_{PAAS}-anomaly (Figure 10f). Seawater has negative Ce_{PAAS}-anomalies due to the
511 large-scale sequestration of Ce^{4+} into hydrogenetic ferromanganese crusts and nodules (Bau,
512 1999; Kato et al., 2006; Ohmoto et al., 2006). If the Ce_{PAAS}-anomalies in Banda Alta Fm BIF are

513 related to the seawater redox condition, then the negative Ce-fractionation supports oxidizing
514 conditions (and an abundance of Ce-sinks) in the Neoproterozoic Jacadigo basin at the time of
515 BIF precipitation. On the other hand, the near absence of Ce_{PAAS}-anomalies in REE II BIF
516 indicates the lack of oxygenated water and/or dissolution of Ce^{4+}-sinks at the time of BIF.
517 Modern oceanic water is redox stratified, affecting the Ce budget of seawater. A continuous
518 decrease of Ce concentration occurs with increasing depth within the upper ~500 m. In addition,
519 or alternatively to oxidative scavenging by hydrogenetic Mn-Fe-hydroxides in the upper marine
520 basins, negative seawater Ce-anomaly recorded in BIF may also be an effect of the REE
521 contribution from large amounts of freshwater: Braun et al. (1990) showed that freshwater is
522 commonly Ce-depleted resulting from weathering-related Ce-enrichment in saprolites and
523 Alexander et al. (2008) show evidence for a significant contribution of continental freshwater
524 solutes to the Nd-isotopic signature in shallow Paleoproterozoic BIF. (Sholkovitz and Schneider,
525 1991; Alibo and Nozaki, 1999). Ce concentrations remain low but largely unchanged also in
526 deeper zones (500 - 3000 m) of the ocean (Alibo and Nozaki, 1999). Contrastingly, in marine
527 sub-basins where hydrological equilibrium with the oceans is incomplete, redoxclines are
528 present, dividing upper oxic and lower anoxic zones (Sholkovitz et al., 1992; Bau et al., 1997).
529 Within and just below the redoxcline, partial Ce^{4+} to Ce^{3+} reduction occurs, increasing the
530 relative solubility, and thus the Ce concentration in water increases by dissolution of Mn-Fe-
531 hydroxides (Bau et al., 1997). In deep anoxic zones, progressed dissolution of hydroxide
532 particles fractionates REE and Y by selective dissolution of LREE over HREE (increase of
533 $(Pr/Yb)_{PAAS}$) and Ho over Y (decrease of Y/Ho), ultimately generating a near-flat dissolved REE
534 pattern with a vanished Ce-anomaly and (no or negative) Y-anomaly (Bau et al., 1997). Those
535 REE trends across three redox zones in relation to a redoxcline has been proposed for

Proterozoic deep marine iron formations associated with partially oxidized seawater (Planavsky et al., 2010). In the present data set, those three zones are represented by the sample set: (1) dolomite-rich BIF and some chert-rich BIF (REE I) representing the oxidized top part above the redoxcline, likely influenced by abundant freshwater; (2) chert-rich BIF and chemically precipitated hematite mud (REE II) from below (but near to) the redoxcline with lower Ce_{PAAS}-anomaly; and (3) hematite chert and hematite mud (REE III), albeit with its contentious detrital and/or volcanic ash contribution, approximating the anoxic "deep" seawater zone characterized by minimal Ce-anomaly and negative Y-anomaly, and maybe influenced by low-temperature hydrothermal fluids (c.f., Planavsky et al., 2010).

In contrast to the "Santa Cruz deposit", Ce_{PAAS}-anomalies in BIF at Morro do Urucum are far less pronounced (Klein and Ladeira, 2004), and in the Rapitan IF even negligible (Halverson et al., 2011; Baldwin et al., 2012), as shown in Figure 11d. In summary, the sample set from the "Santa Cruz deposit" recorded temporarily changing redox conditions in the largely isolated Jacadigo basin, which may be related to fluctuation of the seawater level and associated redoxcline, or variation in fluid-mixing (as discussed in the following section).

9.2. **Fertilization by crustal alteration: hydrothermalism or benthic pore water flux?**

Based on the trace element variations and total values it is suggested that REE II chert-hematite BIF samples recorded a stronger signature of submarine crustal alteration than REE I chert- and dolomite-hematite BIF samples. In cases of pure BIF, an explanation for variations in base metal concentrations are variable fertilization of seawater with metals derived from submarine hydrothermal fluids, benthic pore water flux, or continental solutes. Owing to the lack of Ce_{PAAS}-anomaly in REE II, fertilization under reduced conditions water is a likely scenario for REE II

558 type BIF and precludes oxidized continental solutes derived from weathering of the continental
559 hinterland. Fertilization of seawater is also indicated by Y/Ho ratios (Figure 12e), which range
560 between seawater-like (>40) and chondrite-like signatures (27 - 35) and thus support metal input
561 to seawater from external fluids. Geochemical modelling by Le Hir et al. (2008) shows an up to
562 four times greater rate of alteration reactions in a CO_2-charged snowball earth ocean, therefore
563 crustal alteration (either by pore water or hydrothermal fluids) must have been significant.
564 Elevated Zn/Co ratios are suitable tracers of such crustal alteration, as Co is largely derived from
565 pure seawater, whereas Zn is sourced from altered rocks (Toth, 1980). In the Banda Alta Fm BIF
566 the Zn/Co ratios range between 1.7 and 6 with higher values recorded in chert-hematite BIF
567 (Figure 12e). These ratios are comparable to those recorded in BIF of the Rapitan IF (Halverson
568 et al., 2011) and consistent with significant metal input from altered rocks. Much higher Zn/Co
569 ratios are recorded in hematite chert and mud (18 and 18.8), which contrast those values from
570 hematitic mud and silt of the Rapitan IF.The altered crust may be oceanic crust (low-LREE, Cu
571 and locally Co in REE II rocks) or granitic basement and shales (Pb, Zn, U in REE II and REE
572 III rocks). If detritus and ash is negligible, then the geochemical signatures in hematite chert and
573 hematite mud are consistent with highest contribution from felsic altered rocks.
574 What is the cause of this submarine crustal alteration: hydrothermal activity or widespread
575 scavenging of seafloor sediments by benthic pore waters? The Fe-isotopic composition has the
576 potential to narrows down the sources of iron and alteration fluids: According to Johnson et al.
577 (2003) there are three factors defining the Fe isotope fractionation in BIF: (1) the compositions
578 of the fluids from which minerals were precipitated, (2) the e□ects of metabolic processing of Fe
579 by bacteria, and (3) mineral-specific equilibrium fractionation. The latter factor can be
580 considered as insignificant, since competing phases are just iron-free SiO_2 and carbonates with

581 only a few percent Fe. The fluid Fe-isotopic composition is unknown, but should be in all BIF of
582 the sequence that same, no matter if dolomite or chert-rich, because the Fe source (i.e., altered
583 Fe-rich rocks in the deeper basin) would not have changed significantly. The δ^{57}Fe isotope in
584 REE II type chert-hematite BIF (-0.71 ‰) and REE III type hematite mud (-0.25 and -0.04 ‰)
585 are consistent with MOR hydrothermal fluids (-0.9 to -0.45: Johnson et al., 2003). This supports
586 the presence of hydrothermal fluids as a medium of seawater fertilization. A slight positive shift
587 in δ^{57}Fe associated with the oxidation of Fe (Johnson et al., 2003) should have affected all BIF
588 similarly and point to a primarily slightly more Fe isotope depleted source. The strong Fe isotope
589 fractionation in REE I type carbonate-rich BIF to low δ^{57}Fe (down to 2.6 ‰) does not match any
590 known iron reservoir (Beard and Johnson, 1999; Johnson et al., 2003) and microbial activity is
591 likely a major factor (see section 10.2).
592 The hydrothermal fertilization model is largely accepted for Archean and Paleoproterozoic BIF,
593 and is based on the common REE fractionation patterns exhibiting positive Eu_{PAAS}-anomalies,
594 which are related to high-temperature hydrothermal solutions (>200 °C) in the REE source
595 (Dymek and Klein, 1988; Danielson et al., 1992; Bau and Möller, 1993; Bau and Dulski, 1996;
596 Bau and Dulski, 1999; Ohmoto et al., 2006; Bolhar and Van Kranendonk, 2007; Planavsky et al.,
597 2010). The Neoproterozoic BIF in the "Santa Cruz deposit" shows REE patterns different to
598 Archean and Paleoproterozoic BIF, particularly the absence of a positive Eu anomaly (Figure
599 11**Error! Reference source not found.**c). This points to the absence of high-temperature
600 hydrothermal alteration (Bau and Dulski, 1999), but does not preclude low-temperature
601 hydrothermal fluids (<150 °C), which do not always show Eu enrichment, as shown in Figure
602 11c (Michard et al., 1993; Alexander et al., 2008). The influence of fertilization of the

603 Neoproterozoic seawater with high-temperature fluids has previously been inferred for the
604 Jacadigo BIF (Graf Jr et al., 1994), where the lack of Eu anomaly was attributed to the fluid
605 interacting with rocks that display a negative Eu-anomaly, such as the granitoids in the basement.
606 Basta et al. (2011) concluded for the Wadi Karim BIF in Egypt, which also lack Eu_{PAAS}-
607 anomalies, that low-temperature hydrothermal fluids interacting with mafic rocks fertilized
608 Neoproterozoic seawater. Although the Jacadigo basin lacks evidence of oceanic crust and
609 exhalative hydrothermal processes, the active graben tectonics (D_{x-1}) in the Corumbá Graben
610 may have introduced hydrothermal fluids from deep seated sources (Dardenne, 1998; Walde and
611 Hagemann, 2007). If fluid flow rates were intense enough, possibly accommodated by
612 glacioeustatic pressurization and depressurization (Kump and Seyfried, 2005), these processes
613 may effectively contribute to the metal fertilization.
614 Laterally widespread seafloor sediment alteration by pore fluids is an alternative process that
615 may have fertilized the seawater with metals that were deposited as Fe- and Mn-rich rocks in the
616 Banda Alta Fm. Distal source regions in deeper parts of the basin are envisaged.Pufahl and Hiatt
617 (2012) proposed that hypothetical pyrite-rich back shales in some anoxic deep water sections
618 may have been a potential reservoir for metals including Fe, Mn, Si, and also base metals, Pb,
619 and U. In reduced seawater that was undersaturated in S such hydrothermal reactions could have
620 taken place. Sulphur-undersaturated Neoproterozoic seawater with consequential low sulphate-
621 reducing bacteria activity, has been discussed as a result of the lack of typically sulphate-rich
622 freshwater supply during glaciation (Hoffman, 2009; Swanson-Hysell et al., 2010).
623 In addition to the submarine alteration process(es), glacial erosion of long-lived and thick
624 regolith may have enhanced iron accumulation in the ocean (Swanson-Hysell et al., 2010).
625 Sediments delivered by icebergs are a significant source of iron (as Fe-hydroxide nanoparticles)

626 to the open oceans (Raiswell et al., 2006). However fertilization by ice-delivered metals is not
627 important here, for two reasons: (1) metal concentration are not higher in REE I type BIF, which
628 should be the case as these BIF are strongest influence by ice and freshwater, and (2) considering
629 illite, as a major Rb host, as being a main component in eroded regolith, the relatively low Rb
630 concentration in BIF of the "Santa Cruz deposit" (Figure 12d) does not support such regolith
631 provenance. However, Rb, as well as Al, Ti, Zr, that are enriched in regolith concentrations are
632 much higher at Morro do Urucum (Klein and Ladeira, 2004), suggesting a variable flux of
633 continental derived detritus across the Jacadigo basin. Also, Baldwin et al. (2012) discussed
634 icebergs as a source for metals in the Rapitan IF, which is consistent with higher Rb/Sr values.

635 ## 10. BIF facies in response to tectonics, climate, transgression, and metal
636 sources

637 The above discussed multi-source signatures of the rocks can be correlated with the stratigraphic
638 sequence of the Banda Alta Fm to determine a chemostratigraphy and the sedimentary setting of
639 the basin. This setting can be discussed in terms of the prevailing tectonics, climate, relative
640 redoxcline variation, and fluid sources. In Figure 13a the discussed chemical proxies to a semi-
641 quantitative, albeit spatially limited, chemostratigraphic model are synthesized.

642 ### 10.1. **A glaciomarine depositional environment**

643 The deposition of the BIF in the Jacadigo Group took place in a glaciomarine environment
644 (Urban et al., 1992). This postulation has been regionally supported by BIF that include
645 dropstones and lonestones and the abundant diamictites in the sequence. The negative $\delta^{13}C$
646 values of carbonates in BIF ranging from -3.4 to -7.0 ‰ (also recorded at Morro do Urucum:

647 Klein and Ladeira, 2004), are consistent with signatures from global syn-glacial deposits
648 (Kaufman and Knoll, 1995). Negative $\delta^{13}C_{CARB}$ excursions in stratigraphic carbonates are
649 recorded closely below, within, and closely above Marinoan and Ediacarian glaciogenic
650 sedimentary successions (Kaufman and Knoll, 1995; Swanson-Hysell et al., 2010). According to
651 Kaufman et al. (1991) several possible mechanisms may have contributed to the recorded ^{13}C
652 depletion, of which (1) the breakdown of marine stratification (or upwelling) and mixing of ^{13}C-
653 depleted deep water into the surface ocean, and (2) the erosion of organic-rich rocks exposed
654 during low sea-level (i.e., syn-glaciation) stands are most likely deeper marine water as the
655 predominant source of light C agrees with the proposed Fe source area within the Jacadigo basin.
656 Organic-rich black shales (as metal sources) in the deep parts of the basin have been postulated
657 by Pufahl and Hiatt (2012). Microbial activity in the carbonate precipitation will be discussed in
658 the following section. It is possibly that several processes contributed to the ^{13}C depleted isotope
659 signatures in the glaciogenic successions (Kaufman and Knoll, 1995). Without further, more
660 detailed investigation, the actual cause for the present ^{13}C depleted signatures in the Banda Alta
661 Fm carbonate-rich BIF remains speculative, and the discrepancy in $^{13}C_{CARB}$ between the two
662 putatively coeval glaciogenic sequences, Rapitan IF and Banda Alta Fm BIF remarkable, but
663 unexplained.
664 A glaciomarine precipitation model in response to a redoxcline is based on the present
665 investigation, and largely compatible with the Urban et al. (1992) model (Figure 13b): During
666 glaciation phases, glaciers and sea ice closed-up the basin preventing atmospheric O_2 ventilation.
667 Under such conditions a redoxcline built up, and metals deriving from submarine rock alteration
668 remained largely in solution throughout the basin. A near-complete covering with ice during

669 peak glaciations and a minimized hydrological exchange with the ocean requires the basin being
670 relatively small, like a gulf, and silled (i.e. isolated only in the lower part by graben), as
671 envisaged for the Rapitan IF (Baldwin et al., 2012). In times of glacial retraction, oxidizing
672 conditions in the gulf led to the precipitation of hydroxides rich in Fe^{3+} or Si^{4+} and/or calcium
673 carbonate to form BIF. Carbonate or chert precipitation in BIF was likely in response to
674 prevailing water depth. At the same time, melting of sea ice introduced previously locked-in drop
675 stones and thin clastic layers.

676 10.2. **Hematite and dolomitic carbonate precipitation in response to microbial mediation?**

677 Based on the clear stratigraphic setting (lower and upper dolomite-rich BIF) and the low-$^{13}\delta C$
678 signature of dolomite, it is concluded that carbonates in the Banda Alta Fm BIF derived from
679 seawater precipitation, although most of the carbonate is present as recrystallized Fe-Mn-
680 dolomite ± Fe-Mn-calcite. The Fe-Mn enrichment of the carbonates result from the metal-
681 endowed fluid-rock system in which carbonate was precipitated or recrystallized.
682 The degree of $CaCO_3$ and $Ca(Mg,Fe,Mn)(CO_3)_2$ saturation increases with warming, which is the
683 reason why Phanerozoic and modern shallow-water carbonates exist mainly within 35° of the
684 paleoequator (Kiessling, 2001; Kiessling et al., 2003, and references therein). Therefore, the
685 warmer interglacial periods are the likely setting for carbonate precipitation. Supersaturation of
686 dissolved CO_2 or CO_3^- is required to chemically deposit carbonate (Dupraz et al., 2009, and
687 references therein). There is evidence for higher CO_2 partial pressure in the Neoproterozoic
688 atmosphere compared to recent times (Bao et al., 2008). However, it is questionable if this CO_2
689 concentration had an impact on the restricted carbonate precipitation in the BIF sequences.
690 Therefore, on top of the climatically controlled, elevated CO_2 level, crustal alteration by low-

691 temperature hydrothermal fluids or pore waters likely fertilized seawater with CH_4 or CO_2.
692 Similar provenance for CO_2 has been concluded for Archean-Early Proterozoic carbonate-facies
693 BIF in the Quadrilatero Ferrífero in Brazil, in which dolomite precipitated at shallow depth from
694 seawater that was fertilized with hydrothermal fluids enriched in CO_2 and with a high Mg/Ca
695 ratio (Morgan et al., 2013). A primary precipitation of dolomite remains controversial. One
696 largely accepted model is that dolomite formed by secondary replacement of meta-stable calcium
697 carbonates (aragonite and high-Mg calcite) facilitated by the circulation of (typically Mg-rich)
698 seawater during diagenesis (McKenzie and Vasconcelos, 2009, and references therein).
699 Another (or further) probable process facilitating carbonate precipitation (aragonite, calcite or
700 dolomite) was bacterial activity. Petrographic evidence for microbial activity is the abundance of
701 spheroids. Spheroids are commonly observed in very-low metamorphic grade BIF of various
702 ages (c.f., Krapež et al., 2003; Rasmussen et al., 2013), and biomineralized carbonate with
703 spheroid morphology has been found in diverse modern environments and in geological
704 dolomite samples (McKenzie and Vasconcelos, 2009, and references therein). Mg-calcite
705 microbialites from modern and Devonian reefs (Webb and Kamber, 2000; Nothdurft et al., 2004)
706 have REE pattern characterized by a shallower LREE fractionation trend compared to ambient
707 seawater, therefore most similar to the carbonate-rich BIF (Figure 11a).
708 Calcium carbonate spheroids are discussed as biogenic features linked to cyanobacterial activity
709 involving photosynthetic uptake of dissolved CO_2 or HCO^{3-} facilitating $CaCO_3$ precipitation
710 (c.f., Verrecchia et al., 1995). Such photosynthetic microbial activity and carbonate precipitation
711 is envisaged in interglacial periods by the largely absence of sea ice. Biomediated dolomite
712 precipitation has been shown to occur in various, hypersaline marine settings: Wright and Wacey
713 (2005) proposed dolomite formation through bacterial sulphate reduction. However, this process

714 requiring a sulphate-rich, reduced water-sediment interface was most likely not the key process
715 in the oxidized Banda Alta Fm BIF showing negative Ce_{PAAS}-anomalies and Fe^{3+} in hematite.
716 Also, Neoproterozoic seawater was largely sulphur-undersaturated (Hoffman, 2009; Swanson-
717 Hysell et al., 2010), although during interglacial periods seawater may have been temporarily
718 refertilized with sulphate from freshwater runoffs. The more likely process is microbial dolomite
719 precipitation by aerobic respiration as shown by Sánchez-Román et al. (2009) in the younger
720 geological record and by experiments.
721 Fractionation to negative hematite $\delta^{57}Fe$ values in the carbonate-rich facies BIF supports
722 microbial activity also being active during Fe-hydroxide precipitation. Beard and Johnson (1999)
723 proposed that bacterial metabolism played a crucial role for Fe isotope fractionation during
724 precipitation of marine hydrogenic Fe-Mn nodules and Fe-rich layers in BIF. As the overall
725 source of Fe in all BIF should be the same across the Banda Alta Fm, the dominant process
726 leading to a variation in Fe isotopic composition between dolomite- or chert-rich BIF must be a
727 syn-sedimentary or early diagenetic. In light of the above discussed carbonate genesis, this
728 fractionating process is most likely microbial activity accumulating light ^{57}Fe in iron oxides.
729 Consequently, microbial activity was reduced during precipitation of carbonate-free BIF, mud,
730 and chert; albeit it was still active, mediating Fe oxidation and causing the observed minor ^{57}Fe
731 fractionation.
732 A variability of microbial activity during BIF precipitation in response to temperature changes
733 has been suggested by Posth et al. (2008), who determined experimentally a maximum of bio-
734 mediated Fe-oxidation (and thus Fe-hydroxide precipitation) at 20-25 °C. Conclusively, primary
735 carbonate (dolomite or metastable Mg-Calcite or aragonite) and associated hematite in the Banda
736 Alta Fm BIF was mainly a product of marine biomineralization by aerobic respiration of

737 microbial colonies in warm interglacial, shallow, saline water environment. In the colder and
738 anoxic chert-BIF facies, biomineralization of Fe-hydroxides was also active but reduced.

739 10.3. **A transgression-regression cycle in response to glacial isostatic adjustment**

740 The up-stratigraphy transition in the Banda Alta Fm from a lower carbonate-rich facies to an
741 intermediate jaspilitic BIF facies, via a transitional zone of ~50 metres, in which both facies are
742 alternating, corresponds with simultaneous increase in $\delta^{57}Fe$ value, Zn/Co ratio, Ce_{PAAS}-
743 anomaly, and decrease of $(Pr/Sm)_{PAAS}$ ratio (Figure 13a, b). These geochemical indicators reflect
744 an increase of metal contribution from submarine rock alteration (base metals), or in turn the lack
745 of continental solutes (Ce), and the decrease of microbial activity in the basin below the
746 redoxcline ($\delta^{57}Fe$). Similarly, a covariance of Zn/Co and positive $\delta^{57}Fe$ fractionation (and Y/Ho),
747 all coupled to an increase in water depth, have been observed in the Rapitan IF (Halverson et al.,
748 2011). The $\delta^{57}Fe$ trend in the Rapitan IF is interpreted as an isotopic gradient in the marine water
749 column, in which isotopically heavy Fe is enriched in the lower parts of a chemocline, as a result
750 of upward Fe-diffusion (Halverson et al., 2011). In the Banda Alta Fm BIF, however, heavy Fe is
751 absent and isotope fractionation to light Fe is rather controlled by microbial activity.
752 The proposed up-sequence facies change is compatible with an overall transgressive scenario,
753 initiated with the facies transition from the Urucum Fm (more fluvial) to Córrego das Pedras Fm
754 (more shallow marine with abundant Mn-horizons). In the upper Banda Alta Fm, carbonate-rich
755 BIF indicate the reversed process, i.e., regression of the ocean water. Figure 13c correlates all
756 established climatic, chemical, petrographic parameters to a consistent time-resolved scheme.
757 This scenario is largely compatible with the three-stage basin evolution of the (gulf-like)
758 Jacadigo basin within a half graben proposed by Freitas et al. (2011): During the early rift climax

system tract, the Urucum Fm, characterized by bedload-dominated river, lacustrine and fan-delta environments, was deposited (Freitas et al., 2011). During the mid-rift system tract, the shallow marine Córrego das Pedras Fm and shallow to deeper marine Banda Alta Fm BIF-diamictite facies were the main elements of the basin infill. Based on geochemistry supporting strongest metal fertilization and least oxidation, hematite chert and mud may represent the deepest marine setting, and thus marked, together with the associated middle diamictite, the peak of transgression. After deposition of the upper carbonate-BIF during the regressive stage, the late (post-rift) systems tract caused the extensive carbonate deposits of the Corumbá Group. The stratigraphic column in the Rapitan IF indicates a similar depositional environment related to a relative rise in sea level, and is interpreted as the result of glacial isostatic adjustment during the advance of ice sheets (Klein and Beukes, 1993). If the transgression of the Jacadigo basin was dominated by glacial isostatic adjustment (Lambeck et al., 2014, and references therein), and not (only) by global eustatic sea level rise or regional graben tectonics, then the chert-rich BIF facies marking the transgressive peak is consistent with the peak of the ice age.

10.4. **Diamictites as a gravitation flow of a reworked till**

A direct glaciogenic origin of the diamictites has previously been invoked (Dorr II, 1945; Urban et al., 1992), based on similarities to till sediments. However, the proposed location in the deeper basin of the middle diamictite causes problems related to its genesis. A till pushed forward into the basin during glacial advances is expected only in a near-shore environment, and therefore an unlikely option considering the established deeper basin setting of contemporaneous hematite chert and mud. An alternative scenario compatible with a distal position is the settling of detritus liberated from retracting sea ice. However, this rather slow and continuous scenario is

781 incompatible with the high energy mass flow deduced by the reworked hematite mud breccias in
782 the diamictite footwall. A third possibility is that diamictites represent gravitational flows on the
783 continental margin, possibly triggered by tectonic processes. Such scenario has been proposed
784 for diamictites in the Jacadigo Group (Freitas et al., 2011), and also for similar Neoproterozoic
785 units, e.g., in Namibia (Eyles and Januszczak, 2007). Here we propose the combination of both
786 processes, glaciogenic and gravitational, to be responsible for the middle diamictite
787 sedimentation. Accordingly, diamictites represent a reworked till that was initially pushed by
788 advancing glaciers to a position at the basin slope during the cold peak glacial phase, before it
789 collapsed under its own weight and the glacier's load (or triggered by an earthquake, c.f., Freitas
790 et al., 2011) and moved as a gravitational flow into deeper parts of the basin (Figure 13).
791 Interstitial layers of hematite chert indicate that this process took place several times, with
792 periods of quiescence allowing for chemical chert deposition. Considering a rapid sedimentation
793 of the diamictite flows, the ferruginized and siliceous cement must have been resulted from the
794 abundance of fine reworked iron and chert particles mixed into the diamict slurry.

795 10.5. **The geotectonic setting of the Jacadigo basin - a Brasiliano back arc?**

796 The opening of the Corumbá graben system (c.f., Trompette et al., 1998) in which the Jacadigo
797 Group was deposited, may have been synchronous with deformation during the early Brasiliano
798 collision at ~590 Ma (Trompette et al., 1998 and references therein). According to Freitas et al.
799 (2011), a recorded high-rate subsidence was related to the initiation of the border fault of the
800 (half-) graben system, which implies that the Corumbá graben system was active at least during
801 deposition of the Córrego das Pedras Fm. This is supported by the regionally variable
802 stratigraphic thickness (Trompette et al., 1998) and number of Mn-horizons. In the "Santa Cruz

deposit", the Córrego das Pedras Fm is only a few decametres metres thick, compared with Morro do Urucum, where the Córrego das Pedras Fm is ~90 metres thick (Dorr II, 1945). The entire Jacadigo Group was deposited on the continental shelf of a rifted basin (Walde and Hagemann, 2007), and a likely setting would be a back-arc that was opened during collision related to the Brasiliano orogeny. The discussed low-temperature hydrothermal activity interacting with the basement can be envisaged in a back-arc basin, in which the crust was significantly thinned (Corumbá Graben) and even some volcanic activity may have taken place, as speculated from volcanic ash silicates (?) and metal enrichment in the hematite chert. A continental failed rift basin without production of oceanic crust is envisaged. Similar models involving rifting and contemporaneous exhalation of ore bearing fluids into the basins have been proposed for a series of Neoproterozoic BIF, mainly based on associated mafic rocks in the sequences (i.e. Wadi Karim, Tatonduk, Chestnut Hill, Damara) and/or occur in rifted basins (Chuos, Yerbal, Oraparinna, Holowilena, Braemar, Rapitan BIFs) (Cox et al., 2013, and references therein).

In terms of lateral continuity at the regional scale, it is interesting that BIF in the Morro do Urucum deposit (Klein and Ladeira, 2004) show, at most, weak negative Ce_{PAAS}-anomalies (Figure 11d, Figure 12a**Error! Reference source not found.**). Taking into account that Al, Ti, Zr, and Rb and most base metals concentrations in the Morro do Urucum deposit are much higher (Klein and Ladeira, 2004), and carbonate content in unweathered BIF lower (pers. comm. Rio Tinto staff) than in the "Santa Cruz deposit", this all points to a strong variability of detrital source (and water redox state by glaciogenic water input?) across the Jacadigo basin. The Morro do Urucum deposit was probably located in the less oxygenated, centre of the basin richer in alteration-derived metal, whereas the "Santa Cruz deposit" was located more towards the shore,

826 influenced by oxidized, glaciogenic water in the lower and upper (carbonate-rich) stratigraphic
827 zones.

828 11. Conclusions

829 The present study of the Urucum-type Santa Cruz hematite deposit, successfully contributes to
830 the ongoing discussion of the genesis of Neoproterozoic BIF. A revised depositional model is
831 presented, which supports the sedimentation of complex BIF facies, linked to a tectonically and
832 eustatically controlled transgression-regression cycle under changing climatic and fluid source
833 conditions.
834 Specific geochemical indicators (base metal concentration, Zn/Co ratio, LREE/HREE
835 fractionation, Ce_{PAAS}-anomaly, Y/Ho ratio) in the stratigraphic transition of dolomite-rich to
836 chert-rich BIF to clastic diamictite facies chemical lithologies allows to determine the relative
837 influence of four sources: (1) redox-stratified seawater, (2) base metal-rich fertilizing fluids
838 (low-temperature vent or pore water) derived from altered mafic, felsic, or shale crust, (3)
839 oxidized continental solutes, and (4) terrigenous detritus in silt-layers in BIF and in diamictites.
840 Microbial activity facilitating carbonate precipitation in carbonate-rich BIF in shallow water
841 above a redoxcline is supported by spheroids in carbonate and strongly negative $\delta^{57}Fe$ values in
842 hematite. Whether low-temperature hydrothermal (vent) fluids or (benthic) pore water flux
843 played a dominant role in metal fertilization, remains contentious. The local and regional
844 geological setting suggests that the Jacadigo Group was deposited during active (half-) graben
845 tectonics probably in a continental failed rift back-arc. If this setting is related during initial
846 collisions associated with the Brasiliano orogeny (~590 Ma), then this suggests that the Jacadigo

Group is associated with the suite of Ediacarian glaciations. However, final conclusions on the age of the Jacadigo Group cannot be made.

Figures and Tables

Figure 1: (a) Geological map of the Brasiliano Paraguay fold belt and the Chiquitos-Tucavaca aulacogen which cross-cuts the eastern part of the Amazon craton near the Brazil-Bolivia boundary (according to Schobbenhaus et al., 1981; Litherland et al., 1989; de Alvarenga and Trompette, 1994; Trompette et al., 1998). The contact between the two geological provinces is generally characterized by thrusting of metasediments onto the folded cratonic sequences.

Figure 2: (a) Geological map and (b) cross section of the Corumbá graben system (modified after Walde, 1988; Trompette et al., 1998). Names of the main hills or morros (M): 1. M. do Jacadigo (Mutum in Bolivia); 2. M. da Tromba dos Macacos; 3. M. do Urucum with the underground manganese mine of the Urucum Mineracão; 4. M. Santa Cruz with the São Domingos underground manganese mine (presently inactive), and open-pit iron mine in the northern part; 5. M. Grande with the presently inactive Figueirinha manganese underground mine; 6. M. do Rabichão with the presently inactive Santana manganese underground mine; 7. M. do Zanetti; 8. M. Pelada; 9. M. d'Aguassu; 10. M. do Sajutá.

Figure 3: Generalized stratigraphical profile of the “Santa Cruz deposit”, based on logging and mapping of the authors and company geologists. Stratigraphic nomenclature based on Dorr II (1945).

Figure 4: Cross-section across the “Santa Cruz deposit” (a) NW-SE cross-section; (b) SSW-NNE cross-section. See Figure 5 for map with cross section location.

Figure 5: The “Santa Cruz deposit”; (a) simplified geological map with drill hole locations; (b) four drill hole logs with grab sample locations, including outcrop samples from above drill hole 24-36.

Figure 6: Petrography of dolomite-chert-hematite BIF. (a) sample C-06 with intra-band nodular texture; (b) half core sample showing inter-band pseudonodular dolomite-chert texture; (c) photomicrograph of folded dolomite and chert microbands and hematite-altered spheroids; (d) photomicrograph of a dolomite mesoband showing dolomite-cryptocrystalline hematite nodules in recrystallized dolomite matrix; rims of chert-dolomite-calcite at the contacts between nodules and matrix; cryptocrystalline hematite-rich nodule apex; (e) SEM-backscattered micrograph of a dolomite-chert nodule with cryptocrystalline hematite dust bordered by microcrystalline hematite; (f) photomicrograph of sample C-04 showing two distinct textures in a hematite mesoband: laminae rich in cellular and lepidoblastic microplaty hematite. H = hematite, crxH = cryptocrystalline hematite, TL = transmitted light, RL = reflected light, x = crossed nicols.

Figure 7: Petrography of chert-hematite BIF. (a) banded texture in sample C-14; (b) half core view showing typical dissolution-podding in chert-hematite BIF; (c) photomicrograph of cryptocrystalline hematite-impregnated chert matrix; shown are chert-clast and quartz-veins, both devoid of cryptocrystalline hematite; (d) photomicrograph of sample C-14 showing a cellular hematite mesobands, partly thinned by dissolution-podding; e) photomicrograph of sample C-01 showing fused microplaty hematite texture and potentially clastic remnants; (f) photomicrograph of a gangue layer rich in spheroid and blue stained dolomite. H = hematite, crxH = cryptocrystalline hematite, TL = transmitted light, RL = reflected light, x = crossed nicols.

Figure 8: Petrography of hematite chert and hematite mud; (a) Sample H-03 with red, jaspilitic chert layers and thin hematite laminae; (b) photomicrograph of H-03 with chert layer and hematite lamina; note the hematite-clast in chert; (c) photomicrograph of H-03 showing secondary hematite after fibrous silicates may indicate volcanic ash; (d) photomicrograph of H-03 showing a granular hematite lamina, probably of thixotropic nature; (e) Hematite mud sample H-01 with compact, laminated hematite texture and local chart lenses (f) photomicrograph of H-01 showing irregular fused hematite grains, interpreted as reworked sedimentary texture; (g) photomicrograph of H-01 showing cellular hematite texture; (h) photomicrograph of C-18 showing granoblastic hematite textures (after chemical sedimentation?) with variable grain sizes. H = hematite, crxH = cryptocrystalline hematite, TL = transmitted light, RL = reflected light, x = crossed nicols.

Figure 9: Major element geochemistry of grab samples shown as binary diagrams of major oxides and LOI versus Fe grade. Fields are based on the Vetria assay database (unpublished data, Vetria Mineração). (a) SiO_2 versus Fe shows the unimodal distribution of chert-hematite BIF, inclusive leached BIF, and a clustered distribution of dolomite-chert BIF, which are still relatively rich in SiO_2; (b, c) CaO and MgO are amongst the major constituents only in dolomite-chert-hematite BIF; (d) Al_2O_3 shows the minor contribution of terrigenous material in all samples. The high-Al range in the Vetria database results from inclusion of minor siliciclastic bands into assay samples; (e) P_2O_5 is significantly higher in dolomite-rich BIF resulting in the abundance of apatite grains.

Figure 10: Geochemical tests for the influence of detrital (Al, Ti) and carbonate (Ca) components on trace element patterns, especially the Ce-anomaly. (a) Al_2O_3 versus TiO_2 indicates the general low concentration of terrigenous material in the samples, which is similar to worldwide BIF and

913 Rapitan BIF (Baldwin et al., 2012); see the high concentrations in BIF from the Urucum deposit
914 (Klein and Ladeira, 2004). The worldwide (ww) BIF field is based on a selection of
915 representative BIF across the globe: Temagami BIF, Canada (Bau and Alexander, 2009);
916 Kuruman Iron Formation, South Africa (Gutzmer et al., 2008); Sandur schist belt BIF (Gutzmer
917 et al., 2008), Caué Fm, Quadrilatero Ferrifero, Brazil (Spier et al., 2007); Carajas Serra Norte
918 deposits (Figueiredo e Silva et al., 2008); Koolyanobbing and Windarling deposits, Yilgarn
919 Craton (Angerer et al., 2012; Angerer et al., 2013); Pic de Fon deposit, Guinea (Cope et al.,
920 2008), Brockman and Marra Mamba Iron Formations, Western Australia, including Tom Price,
921 Mt. Whaleback, Eastern Ridge, and Mesa Gap deposits (unpublished data from the first author).
922 (b, c) Al_2O_3 and TiO_2 versus $(Ce/Ca^*)_{PAAS}$ show no significant influence (no covariability) of
923 detrital components on Ce-anomaly; (d) Y/Ho versus Zr indicates a slight covariance across the
924 sample set, but not with the distinct REE groups. See high Zr in hematite chert sample H-03; (e)
925 CaO versus $(Ce/Ce^*)_{PAAS}$ shows that the specific Ce_{PAAS}-anomalies of REE I- and II-type BIF
926 are unrelated to carbonate content (f) Binary diagram of $(Pr/Pr^*)_{PAAS}$ versus $(Ce/Ce^*)_{PAAS}$
927 indicates the ubiquitous presence of a true negative Ce-anomaly in all samples, and the absence
928 of a true La anomaly (cf. Bau and Dulski, 1996; Planavsky et al., 2010).
929 Figure 11: REE multi-element diagrams. (a) REE I type dolomite-chert-hematite and chert-
930 hematite BIF in comparison with modern seawater (Alibo and Nozaki, 1999), modern calcitic
931 microbialites (Webb and Kamber, 2000) and Devonian microbialites (Nothdurft et al., 2004); (b)
932 REE II type chert-(dolomite)-hematite and chemical hematite mud; (c) REE III type hematite
933 chert and reworked hematite mud in comparison with Archean BIF (IF-G: Bolhar et al., 2004),
934 high-temperature vent fluids (Bau and Dulski, 1999) and low-temperature vents fluids (Michard
935 et al., 1993). (d) calculated mean values of carbonate-bearing and carbonate-poor BIF from

936 published datasets: Morro do Urucum (Klein and Ladeira, 2004) and Rapitan IF (Halverson et
937 al., 2011; Baldwin et al., 2012). To ease comparison, all normalized fluid data are multiplied to
938 fit the present scale.
939
940 Figure 12: Binary diagrams for selected major and trace elements (see Figure 10 caption**Error!**
941 **Reference source not found.** for references to fields, additional data for the Rapitan IF (BIF,
942 hematitic mud and hematitic silt) are from Halverson et al. (2011); (a) $(Pr/Yb)_{PAAS}$ versus
943 $(Ce/Ce^*)_{PAAS}$ discriminates the REE pattern I, II, III, but also shows the transition between REE
944 I and REE II. A negative Ce_{PAAS} anomaly is well developed only in REE I type BIF from the
945 "Santa Cruz deposit", (the Urucum dataset of Klein and Ladeira (2004) lacks Pr, hence
946 $(La/Yb)_{PAAS}$ is shown and Ce-anomaly calculated with Nd); (b) discrimination of REE I type BIF
947 from REE II and III types based on low Cu and Pb abundances is a result of the dilution with
948 metal-depleted continental solutes; (c) a correlation of MnO and Co results from hydrogenetic
949 co-precipitation, whereas disturbance of this trend derives from variable hydrothermal Co
950 contribution; (d) a very low Rb/Sr ratio (based on low Rb) in samples of the "Santa Cruz
951 deposit", compared with other BIF, suggests low amount of weathering-derived detritus or
952 solutes from altered continental crust; (e) The combined plot of Zn/Co and Y/Ho discriminates
953 various metal and REE sources. Elevated Zn/Co is a proxy for Zn input by crustal alteration, and
954 the range of Y/Ho shows the mixing of various sources into seawater (continental solutes, crustal
955 alteration, and anoxic deep seawater); (f) Cr covaries with Fe, both being distributed in hematite
956 and passively enriched by dissolution-podding.
957

Figure 13: (a) Chemostratigraphic variations in the BIF facies in the Jacadigo basin as recorded in the "Santa Cruz deposit". See text for discussion. (b) Chemical cycling in the Jacadigo basin: Metals for BIF precipitation derived from upwelling low-temperature hydrothermal solutes or pore water. Formations of the two main BIF facies, carbonate- and chert-rich, were related to the relative position of the seafloor to the redoxcline (transition from oxic to anoxic water), which fluctuated due to transgression juxtaposed with glaciogenic processes. Carbonate and hematite precipitation in the shallow zone above the redoxcline was facilitated by basin-wide CO_2 abundance and bacteria mediation. Chert-rich BIF with stronger hydrothermal signature lacks the contribution of diluting and oxygenated shallow water from melting glaciers, and bacteria activity was still active but reduced. Hematite chert and reworked mud, preceding and following the middle diamictite flow, may represent the deepest zone showing strongest input of metals derived from submarine alteration. (c) simplified variations of basin parameters: The time-dependent variation of the depth of the redoxcline and submarine crustal alteration versus continental solute influxes result from the juxtaposition of the overall marine transgression and shorter-term glacial advance-regression cycles.

Table 1: Sample set (BIF, hematite chert, hematite mud) from the "Santa Cruz deposit".

Table 2: Whole-rock data for representative BIF and chert samples from the "Santa Cruz deposit". The Ce-anomaly $(Ce/Ce^*)_{PAAS}$ is calculated as $Ce_{(PAAS)}/(0.5*La_{PAAS}+0.5*Pr_{PAAS})$, Eu-anomaly $(Eu/Eu^*)_{PAAS}$ is calculated as $Eu_{(PAAS)}/(0.5*Sm_{PAAS}+0.5*Gd_{PAAS})$.

Table 3: Fe isotope data of representative BIF samples. *relative to the IRMM14 standard. § δ^{56}Fe is measured directly on the MC, but can also calculated from δ^{57}Fe (= 2/3* δ^{56}Fe). For comparison, data from Rapitan IF (Halverson et al., 2011) are shown (in stratigraphic sequence).

Table 4: Carbonate δ^{13}C isotope data from the "Santa Cruz deposit". Published data from the Urucum (Klein and Ladeira, 2004) and Rapitan (Klein and Beukes, 1993) deposits are also shown.

Acknowledgements

This study on the genesis of the Santa Cruz iron ore deposit was funded by Vetria Mineração and University of Western Australia. Thanks to Augusto Mendonça for the initiation of the project. We highly acknowledge the technical and logistical support from Leandro Silva and Rafael Henchen. Many thanks go to the very helpful geologists and technical assistants of Coffey Mining, especially Geraldo G. Vieira dos Santos and Davi Saldanha for sharing their sound geological understanding of the deposit. Further thanks go to the involved consultants Profs J.L.H. D'el Rey Silva, N. Souza Gomes, P. César Souza, and E. Hiatt for their insights in form of internal reports. The reviewers Michael Bau and Paulo Boggiani as well as two anonymous reviewers of an early version are greatly acknowledged for their input.

References

Alexander, B.W., Bau, M., 2009. Distribution of high field strengh elements (Y, Zr, REE, Hr, Ta, Th, U) in adjacent magnetite and chert bands in reference standards FeR-3 and FeR-4 from the Temagami iron-formation, Canada, and the redox level of the Neoarchean ocean. Precambrian Research, 174: 337-346.

Alexander, B.W., Bau, M., Andersson, P., Dulski, P., 2008. Continentally-derived solutes in shallow Archean seawater: Rare earth element and Nd isotope evidence in iron formation from the 2.9 Ga Pongola Supergroup, South Africa. Geochimica et Cosmochimica Acta, 72(2): 378-394.

1003 Alibo, D.S., Nozaki, Y., 1999. Rare earth elements in seawater: particle association, shale-
1004 normalization, and Ce oxidation. Geochimica et Cosmochimica Acta, 63(3-4): 363-372.
1005 Angerer, T., Hagemann, S.G., Danyushevsky, L.V., 2012. Geochemical Evolution of the Banded
1006 Iron Formation-Hosted High-Grade Iron Ore System in the Koolyanobbing Greenstone
1007 Belt, Western Australia. Economic Geology, 107(4): 599-644.
1008 Angerer, T., Hagemann, S.G., Danyushevsky, L.V., 2013. High-grade iron ore at Windarling,
1009 Yilgarn Craton: a product of syn-orogenic deformation, hypogene hydrothermal
1010 alteration and supergene modification in an Archean BIF-basalt lithostratigraphy.
1011 Mineralium Deposita, 48(6): 697–728.
1012 Babinski, M., Boggiani, P.C., Trindade, R.I.F., Fanning, C.M., 2013. Detrital zircon ages and
1013 geochronological constraints on the Neoproterozoic Puga diamictites and associated
1014 BIFs in the southern Paraguay Belt, Brazil. Gondwana Research, 23(3): 988-997.
1015 Baldwin, G.J., Turner, E.C., Kamber, B.S., Colpron, M., 2012. A new depositional model for
1016 glaciogenic Neoproterozoic iron formation: insights from the chemostratigraphy and
1017 basin configuration of the Rapitan iron formation 1 1 Northwest Territories Geoscience
1018 Office Contribution 0052. Canadian Journal of Earth Sciences, 49(2): 455-476.
1019 Bao, H., Lyons, J., Zhou, C., 2008. Triple oxygen isotope evidence for elevated CO2 levels after a
1020 Neoproterozoic glaciation. Nature, 453(7194): 504-506.
1021 Barbosa, O., 1949. Contribuicão à geologia da região Brasil-Bolivia, Mineração Metalurgia, Rio
1022 de Janeiro, Brazil, XIII, pp. 271-278.
1023 Basta, F.F., Maurice, A.E., Fontboté, L., Favarger, P.-Y., 2011. Petrology and geochemistry of the
1024 banded iron formation (BIF) of Wadi Karim and Um Anab, Eastern Desert, Egypt:
1025 Implications for the origin of Neoproterozoic BIF. Precambrian Research, 187(3–4): 277-
1026 292.
1027 Bau, M., 1999. Scavenging of dissolved yttrium and rare earths by precipitating iron
1028 oxyhydroxide: experimental evidence for Ce oxidation, Y-Ho fractionation, and
1029 lanthanide tetrad effect. Geochimica et Cosmochimica Acta, 63(1): 67-77.
1030 Bau, M., Alexander, B.W., 2009. Distribution of high field strength elements (Y, Zr, REE, Hf, Ta,
1031 Th, U) in adjacent magnetite and chert bands and in reference standards FeR-3 and FeR-
1032 4 from the Temagami iron-formation, Canada, and the redox level of the Neoarchean
1033 ocean. Precambrian Research, 174(3-4): 337-346.
1034 Bau, M., Dulski, P., 1996. Distribution of yttrium and rare-earth elements in the Penge and
1035 Kuruman iron-formations, Transvaal Supergroup, South Africa. Precambrian Research,
1036 79(1-2): 37-55.
1037 Bau, M., Dulski, P., 1999. Comparing yttrium and rare earths in hydrothermal fluids from the
1038 Mid-Atlantic Ridge: implications for Y and REE behaviour during near-vent mixing and
1039 for the Y/Ho ratio of Proterozoic seawater. Chemical Geology, 155(1-2): 77-90.
1040 Bau, M., Dulski, P., Möller, P., 1995. Yttrium and Holmium in South Pacific Seawater: Vertical
1041 Distribution and Possible Fractionation Mechanisms. Chemie der Erde, 55: 1-15.
1042 Bau, M., Möller, P., 1993. Rare earth element systematics of the chemically precipitated
1043 component in early precambrian iron formations and the evolution of the terrestrial

atmosphere-hydrosphere-lithosphere system. Geochimica et Cosmochimica Acta, 57(10): 2239-2249.

Bau, M., Möller, P., Dulski, P., 1997. Yttrium and lanthanides in eastern Mediterranean seawater and their fractionation during redox-cycling. Marine Chemistry, 56(1): 123-131.

Beard, B.L., Johnson, C.M., 1999. High precision iron isotope measurements of terrestrial and lunar materials. Geochimica et cosmochimica acta, 63(11): 1653-1660.

Beard, B.L., Johnson, C.M., 2004. Fe isotope variations in the modern and ancient earth and other planetary bodies. Reviews in Mineralogy and Geochemistry, 55(1): 319-357.

Bolhar, R., Kamber, B.S., Moorbath, S., Fedo, C.M., Whitehouse, M.J., 2004. Characterisation of early Archaean chemical sediments by trace element signatures. Earth and Planetary Science Letters, 222(1): 43-60.

Bolhar, R., Van Kranendonk, M.J., 2007. A non-marine depositional setting for the northern Fortescue Group, Pilbara Craton, inferred from trace element geochemistry of stromatolitic carbonates. Precambrian Research, 155(3-4): 229-250.

Bowring, S., Myrow, P., Landing, E., Remezani, J., Grotzinger, J., 2003. Geochronological constraints on terminal Neoproterozoic events and the rise of metazoans. Geophysical Research Abstracts, 5: 13219.

Braun, J.-J. et al., 1990. Cerium anomalies in lateritic profiles. Geochimica et Cosmochimica Acta, 54(3): 781-795.

Cope, I.L. et al., 2008. Genesis of the Pic de Fon Iron Oxide Deposit, Simandou Range, Republic of Guinea, West Afrika. Reviews in Economic Geology, 15: 339-360.

Cox, G.M. et al., 2013. Neoproterozoic iron formation: An evaluation of its temporal, environmental and tectonic significance. Chemical Geology, 362: 232-249.

D'el-Rey Silva, L.J.H., Walde, D.H.G., Saldanha, D.O., in press. New Structural Data and a New Approach on the Tectonic Evolution of the Paraguay Belt (Neoproterozoic-Cambrian of central Brazil). Tectonophysics.

Danielson, A., Möller, P., Dulski, P., 1992. The europium anomalies in banded iron formations and the thermal history of the oceanic crust. Chemical Geology, 97(1-2): 89-100.

Dardenne, M., 1998. Modelo hidrotermal-exhalativo para os depósitos de Fe-Mn da região de Corumbá, Mato Grosso do Sul, 40. Congresso Brasileiro de Geologia, Anais, São Paulo (SBG).

de Almeida, F.F.M., 1945. Geologia do sudoeste mato grossense. Bol. Dep. Nac. Prod. Mineral, 116: 1-118.

de Alvarenga, C.J.S., Trompette, R., 1994. A Faixa Paraguai e a sua compartimentação estratigráfica e tectônica, 388 Cong. Brasil. Geol., Camboriú Bol. Resumos expandidos pp. 229-230.

Dorr II, J.V.N., 1945. Manganese and Iron Deposits of Morro Do Urucum, Mato Grosso, Brazil, Bulletin of the United States Geological Survey, pp. 1-47.

Dupraz, C. et al., 2009. Processes of carbonate precipitation in modern microbial mats. Earth-Science Reviews, 96(3): 141-162.

1085 Dymek, R.F., Klein, C., 1988. Chemistry, petrology and origin of banded iron-formation
1086 lithologies from the 3800 MA isua supracrustal belt, West Greenland. Precambrian
1087 Research, 39(4): 247-302.
1088 Eyles, N., Januszczak, N., 2007. Syntectonic subaqueous mass flows of the Neoproterozoic Otavi
1089 Group, Namibia: where is the evidence of global glaciation? Basin Research, 19(2): 179-
1090 198.
1091 Figueiredo e Silva, R.C., Lobato, L.M., Rosiere, C.A., 2008. A Hydrothermal Origin for the
1092 Jaspilite-Hosted Giant Sierra Norte Deposits in the Cajajas Mineral Province, Para State,
1093 Brazil. Reviews in Economic Geology, 15: 255-290.
1094 Freitas, B.T., Warren, L.V., Boggiani, P.C., De Almeida, R.P., Piacentini, T., 2011. Tectono-
1095 sedimentary evolution of the Neoproterozoic BIF-bearing Jacadigo Group, SW-Brazil.
1096 Sedimentary Geology, 238(1–2): 48-70.
1097 Graf Jr, J.L., O'Connor, E.A., van Leeuwen, P., 1994. Rare earth element evidence of origin and
1098 depositional environment of Late Proterozoic ironstone beds and manganese-oxide
1099 deposits, SW Brazil and SE Bolivia. Journal of South American Earth Sciences, 7(2): 115-
1100 133.
1101 Gutzmer, J., Chisonga, C.B., Beukes, N.J., Mukhopadhyay, J., 2008. The Geochemistry of Iron
1102 Formation-Hosted High-Grade Hematite-Martite Iron Ores. Reviews in Economic
1103 Geology, 15: 157-183.
1104 Halverson, G.P. et al., 2011. Fe isotope and trace element geochemistry of the Neoproterozoic
1105 syn-glacial Rapitan iron formation. Earth and Planetary Science Letters, 309(1–2): 100-
1106 112.
1107 Hasui, Y., Almeida, F.d., 1970. Geocronologia do centro-oeste brasileiro. Boletim da Sociedade
1108 Brasileira de Geologia, 19(1): 5-26.
1109 Hensler, A.-S., Hagemann, S.G., Rosière, C.A., Angerer, T., Gilbert, S., 2015. Hydrothermal and
1110 metamorphic fluid-rock interaction associated with hypogene “hard” iron ore
1111 mineralisation in the Quadrilátero Ferrífero, Brazil: Implications from in-situ laser
1112 ablation ICP-MS iron oxide chemistry. Ore Geology Reviews(0).
1113 Hoffman, P.F., 2009. Pan-glacial—a third state in the climate system. Geology Today, 25(3):
1114 100-107.
1115 Hoffman, P.F., Kaufman, A.J., Halverson, G.P., Schrag, D.P., 1998. A Neoproterozoic snowball
1116 Earth. Science, 281: 1342-1346.
1117 Hoffman, P.F., Li, Z.-X., 2009. A palaeogeographic context for Neoproterozoic glaciation.
1118 Palaeogeography, Palaeoclimatology, Palaeoecology, 277(3–4): 158-172.
1119 Hoffman, P.F., Macdonald, F.A., Halverson, G.P., 2011. Chemical sediments associated with
1120 Neoproterozoic glaciation: iron formation, cap carbonate, barite and phosphorite. In: E.
1121 Arnaud, G.P. Halverson and G. Shields-Zhou (Editors), The Geological Record of
1122 Neoproterozoic Glaciations. Geological Society, London, Memoirs, pp. 67-80.
1123 Johnson, C.M., Beard, B.L., Beukes, N.J., Klein, C., O'Leary, J.M., 2003. Ancient geochemical
1124 cycling in the Earth as inferred from Fe isotope studies of banded iron formations from
1125 the Transvaal Craton. Contributions to Mineralogy and Petrology, 144(5): 523-547.

1126 Jones, J.P., 1985. The southern border of the Guaporé Shield in western Brazil and Bolivia: An
1127 interpretation of its geologic evolution. Precambrian Research, 28(2): 111-135.
1128 Kato, Y., Yamaguchi, K.E., Ohmoto, H., 2006. Rare earth elements in Precambrian banded iron
1129 formations: Secular changes of Ce and Eu anomalies and evolution of atmospheric
1130 oxygen. In: S. Kesler and H. Ohmoto (Editors), Evolution of the Atmosphere,
1131 Hydrosphere, and Biosphere on Early Earth: Constraints from Ore Deposits. Geological
1132 Society of America Memoir, 196, pp. 269-289.
1133 Kaufman, A.J., Hayes, J., Knoll, A.H., Germs, G.J., 1991. Isotopic compositions of carbonates and
1134 organic carbon from upper Proterozoic successions in Namibia: stratigraphic variation
1135 and the effects of diagenesis and metamorphism. Precambrian Research, 49(3): 301-
1136 327.
1137 Kaufman, A.J., Knoll, A.H., 1995. Neoproterozoic variations in the C-isotopic composition of
1138 seawater: stratigraphic and biogeochemical implications. Precambrian Research, 73(1):
1139 27-49.
1140 Kiessling, W., 2001. Paleoclimatic significance of Phanerozoic reefs. Geology, 29(8): 751-754.
1141 Kiessling, W., Flügel, E., Golonka, J., 2003. Patterns of Phanerozoic carbonate platform
1142 sedimentation. Lethaia, 36(3): 195-225.
1143 Klein, C., 1974. Greenalite, stilpnomelane, minnesotaite, crocidolite, and carbonates in very
1144 low-grade metamorphic Precambrian iron-formation. Canadian Mineralogist, 12: 475-
1145 498.
1146 Klein, C., 2005. Some Precambrian banded iron-formations (BIFs) from around the world: Their
1147 age, geologic setting, mineralogy, metamorphism, geochemistry, and origin. American
1148 Mineralogist, 90(10): 1473-1499.
1149 Klein, C., Beukes, N.J., 1993. Sedimentology and Geochemistry of the Glaciogenic Late
1150 Proterozoic Rapitan Iron-Formation in Canada. Economic Geology, 88: 542-565.
1151 Klein, C., Ladeira, E.A., 2004. Geochemistry and Mineralogy of Neoproterozoic Banded Iron-
1152 Formations and some selected, Siliceous Manganese Formations from the Urucum
1153 District, Mato Grosso do Sul, Brazil. Economic Geology, 99(6): 1233-1244.
1154 Krapež, B., Barley, M.E., Pickard, A.L., 2003. Hydrothermal and resedimented origins of the
1155 precursor sediments to banded iron formation: sedimentological evidence from the
1156 Early Palaeoproterozoic Brockman Supersequence of Western Australia. Sedimentology,
1157 50(5): 979-1011.
1158 Kump, L.R., Seyfried, W.E., 2005. Hydrothermal Fe fluxes during the Precambrian: effect of low
1159 oceanic sulfate concentrations and low hydrostatic pressure on the composition of black
1160 smokers. Earth and Planetary Science Letters, 235(3): 654-662.
1161 Lambeck, K., Rouby, H., Purcell, A., Sun, Y., Sambridge, M., 2014. Sea level and global ice
1162 volumes from the Last Glacial Maximum to the Holocene. Proceedings of the National
1163 Academy of Sciences, 111(43): 15296-15303.
1164 Le Hir, G., Ramstein, G., Donnadieu, Y., Goddéris, Y., 2008. Scenario for the evolution of
1165 atmospheric pCO2 during a snowball Earth. Geology, 36(1): 47-50.
1166 Litherland, M. et al., 1986. The geology and mineral resources of the Bolivian Precambrian
1167 shield. British Geol. Surv., Overseas Memoirs, 9: 1-153.

1168 Litherland, M. et al., 1989. The proterozoic of Eastern Bolivia and its relationship to the Andean
1169 mobile belt. Precambrian Research, 43(3): 157-174.
1170 Macdonald, F.A. et al., 2010. Calibrating the cryogenian. Science, 327(5970): 1241-1243.
1171 McKenzie, J.A., Vasconcelos, C., 2009. Dolomite Mountains and the origin of the dolomite rock
1172 of which they mainly consist: historical developments and new perspectives.
1173 Sedimentology, 56(1): 205-219.
1174 Michard, A. et al., 1993. Submarine thermal springs associated with young volcanoes: The
1175 Teahitia vents, Society Islands, Pacific Ocean. Geochimica et Cosmochimica Acta, 57(21–
1176 22): 4977-4986.
1177 Morgan, R. et al., 2013. The origin of coexisting carbonates in banded iron formations: A micro-
1178 mineralogical study of the 2.4 Ga Itabira Group, Brazil. Precambrian Research,
1179 224(0): 491-511.
1180 Nadoll, P., Angerer, T., Mauk, J.L., French, D., Walshe, J., 2014. The Chemistry of hydrothermal
1181 magnetite: A review. Ore Geology Reviews.
1182 Nothdurft, L.D., Webb, G.E., Kamber, B.S., 2004. Rare earth element geochemistry of Late
1183 Devonian reefal carbonates, Canning Basin, Western Australia: confirmation of a
1184 seawater REE proxy in ancient limestones. Geochimica et Cosmochimica Acta, 68(2):
1185 263-283.
1186 O'Connor, E.A., Walde, D.H.G., 1985. Recognition of an Eocambrian orogenic cycle in SW Brazil
1187 and SE Bolivia. Zentralbl. Geol. Paläont., 1: 1441-1456.
1188 Ohmoto, H. et al., 2006. Chemical and biological evolution of early Earth: Constraints from
1189 banded iron-formations. In: S. Kesler and H. Ohmoto (Editors), Evolution of the
1190 Atmosphere, Hydrosphere, and Biosphere on Early Earth: Constraints from Ore
1191 Deposits. Geological Society of America Memoir, 196, pp. 291-331.
1192 Owen, G., 2003. Load structures: gravity-driven sediment mobilization in the shallow
1193 subsurface. Geological Society, London, Special Publications, 216(1): 21-34.
1194 Pack, A., Russell, S.S., Shelley, J.M.G., van Zuilen, M., 2007. Geo- and cosmochemistry of the
1195 twin elements yttrium and holmium. Geochimica et Cosmochimica Acta, 71(18): 4592-
1196 4608.
1197 Pearce, C.R., Jones, M.T., Oelkers, E.H., Pradoux, C., Jeandel, C., 2013. The effect of particulate
1198 dissolution on the neodymium (Nd) isotope and Rare Earth Element (REE) composition
1199 of seawater. Earth and Planetary Science Letters, 369–370: 138-147.
1200 Piacentini, T., Vasconcelos, P.M., Farley, K.A., 2013. 40Ar/39Ar constraints on the age and
1201 thermal history of the Urucum Neoproterozoic banded iron-formation, Brazil.
1202 Precambrian Research, 228(0): 48-62.
1203 Pimentel, K.M.R., Fuck, R.A., 1992. Neoproterozoic crustal accretion in central Brazil. Geology,
1204 20: 375-379.
1205 Pimentel, M.M., Fuck, R.A., de Alvarenga, C.J., 1996. Post-Brasiliano (Pan-African) high-K
1206 granitic magmatism in Central Brazil: the role of late Precambrian-early Palaeozoic
1207 extension. Precambrian Research, 80(3–4): 217-238.

1208 Planavsky, N. et al., 2010. Rare Earth Element and yttrium compositions of Archean and
1209 Paleoproterozoic Fe formations revisited: New perspectives on the significance and
1210 mechanisms of deposition. Geochimica et Cosmochimica Acta, 74(22): 6387-6405.
1211 Posth, N.R., Hegler, F., Konhauser, K.O., Kappler, A., 2008. Alternating Si and Fe deposition
1212 caused by temperature fluctuations in Precambrian oceans. Nature Geoscience, 1(10):
1213 703-708.
1214 Pufahl, P.K., Hiatt, E.E., 2012. Oxygenation of the Earth's atmosphere–ocean system: A review
1215 of physical and chemical sedimentologic responses. Marine and Petroleum Geology,
1216 32(1): 1-20.
1217 Raiswell, R. et al., 2006. Contributions from glacially derived sediment to the global iron
1218 (oxyhydr) oxide cycle: implications for iron delivery to the oceans. Geochimica et
1219 Cosmochimica Acta, 70(11): 2765-2780.
1220 Rasmussen, B., Meier, D.B., Krapež, B., Muhling, J.R., 2013. Iron silicate microgranules as
1221 precursor sediments to 2.5-billion-year-old banded iron formations. Geology, 41(4):
1222 435-438.
1223 Sánchez-Román, M., Vasconcelos, C., Warthmann, R., Rivadeneyra, M., McKenzie, J.A., 2009.
1224 Microbial Dolomite Precipitation under Aerobic Conditions: Results from Brejo do
1225 Espinho Lagoon (Brazil) and Culture Experiments: IAS Spec Publ, vol. 41. Perspectives in
1226 Carbonate Geology: A Tribute to the Career of Robert Nathan Ginsburg: 167-178.
1227 Schneider, G., 1984. Zur Mineralogie und Lagerstättenbildung der Mangan- und
1228 Eisenerzvorkommen des Urucum-Distriktes (Mato Grosso do Sul, Brasilien), 1. Johann
1229 Wolfgang Goethe-Universität Frankfurt, Frankfurter Geowissenschaftliche Arbeiten,
1230 Serie C Mineralogie, 202 pp.
1231 Schobbenhaus, C., Campos, D.A., Derze, G.R., Asmus, H.E., 1981. Mapa geológico do Brasil e da
1232 área oceânica adjacente incluindo depósitos minerais. Escala 1/2.500.000, Dep. Nac.
1233 Produc°. Mineral (D.N.P.M.), Brasilia.
1234 Schreck, P.C., 1984. Geochemische Klassifikat.ion und Petrogenese der Manganerze des
1235 Urucum-Distriktes bei Corumba (Mato Grosso do Sul, Brasilien), 3. Johann Wolfgang
1236 Goethe-Universität Frankfurt, Frankfurter Geowissenschaftliche Arbeiten, Serie C
1237 Mineralogie, 206 pp.
1238 Severmann, S., Johnson, C.M., Beard, B.L., McManus, J., 2006. The effect of early diagenesis on
1239 the Fe isotope compositions of porewaters and authigenic minerals in continental
1240 margin sediments. Geochimica et Cosmochimica Acta, 70(8).
1241 Shannon, R., 1976. Revised effective ionic radii and systematic studies of interatomic distances
1242 in halides and chalcogenides. Acta Crystallographica Section A, 32(5): 751-767.
1243 Shiraiwa, S., 1994. Flexura da litosfera continental sob os Andes centrais e a origem da bacia do
1244 Pantanal. Tese dout, 91 pp.
1245 Sholkovitz, E., Shaw, T.J., Schneider, D., 1992. The geochemistry of rare earth elements in the
1246 seasonally anoxic water column and porewaters of Chesapeake Bay. Geochimica et
1247 Cosmochimica Acta, 56(9): 3389-3402.
1248 Sholkovitz, E.R., Schneider, D.L., 1991. Cerium redox cycles and rare earth elements in the
1249 Sargasso Sea. Geochimica et Cosmochimica Acta, 55(10): 2737-2743.

Skulan, J.L., Beard, B.L., Johnson, C.M., 2002. Kinetic and equilibrium Fe isotope fractionation between aqueous Fe (III) and hematite. Geochimica et Cosmochimica Acta, 66(17): 2995-3015.

Spier, C.A., de Oliveira, S.M.B., Sial, A.N., Rios, F.J., 2007. Geochemistry and genesis of the banded iron formations of the Cauê Formation, Quadrilátero Ferrífero, Minas Gerais, Brazil. Precambrian Research, 152(3-4): 170-206.

Swanson-Hysell, N.L. et al., 2010. Cryogenian glaciation and the onset of carbon-isotope decoupling. Science, 328(5978): 608-611.

Tepe, N., Bau, M., 2014. Importance of nanoparticles and colloids from volcanic ash for riverine transport of trace elements to the ocean: Evidence from glacial-fed rivers after the 2010 eruption of Eyjafjallajökull Volcano, Iceland. Science of The Total Environment, 488–489: 243-251.

Toth, J.R., 1980. Deposition of submarine crusts rich in manganese and iron. Geological Society of America Bulletin, 91(1): 44-54.

Trompette, R., de Alvarenga, C.J.S., Walde, D., 1998. Geological evolution of the Neoproterozoic Corumbágraben system (Brazil). Depositional context of the stratified Fe and Mn ores of the Jacadigo Group. Journal of South American Earth Sciences, 11(6): 587-597.

Urban, H., Stribrny, B., Lippolt, H.J., 1992. Iron and manganese deposits of the Urucum District, Mato Grosso do Sul, Brazil. Economic Geology, 87(5): 1375-1392.

Ussami, N., Shiraiwa, S., Dominguez, J.M.L., 1999. Basement reactivation in a sub-Andean foreland flexural bulge: The Pantanal wetland, SW Brazil. Tectonics, 18(1): 25-39.

Verrecchia, E.P., Freytet, P., Verrecchia, K.E., Dumont, J.-L., 1995. Spherulites in calcrete laminar crusts: biogenic CaCO3 precipitation as a major contributor to crust formation. Journal of Sedimentary Research, 65(4).

Walde, D., 1988. Das Proterozoische Paraguay-Araguaia orogen in West-Brasilien, ausgehend von untersuchungen im Raum Corumbá, Habilitationsschrift, unpubished, Albert-Ludwigs University, Freiburg, 122 pp.

Walde, D., Hagemann, S.G., 2007. The Neoproterozoic Urucum/Mutún Fe and Mn deposits in W-Brazil/SE-Bolivia: assessment of ore deposit models. Z. dt. Ges. Geowiss., 158(1): 45-55.

Walde, D.H. et al., 2015. New aspects of Neoproterozoic-Cambrian transition in the Corumbá region (state of Mato Grosso do Sul, Brazil), Annales de Paléontologie. Elsevier, pp. 213-224.

Webb, G.E., Kamber, B.S., 2000. Rare earth elements in Holocene reefal microbialites: a new shallow seawater proxy. Geochimica et Cosmochimica Acta, 64(9): 1557-1565.

Wright, D.T., Wacey, D., 2005. Precipitation of dolomite using sulphate-reducing bacteria from the Coorong Region, South Australia: significance and implications. Sedimentology, 52(5): 987-1008.

sample_ID	locality	BIF facies	lithology	Vetria core STCR-DD-	core depth	BIF texture	REE pattern	geochemistry	Fe isotope (hematite)	C & O isotope (mineral)	comparible samples	References
H-03	Santa Cruz	intermed. siliceous	hematite chert	outcrop	-	-	III	yes	-	-		this study
H-01	Santa Cruz	intermed. siliceous	reworked hematite mud	outcrop	-	-	III	yes	-	-	a	this study
H-15	Santa Cruz	intermed. siliceous	reworked hematite mud	outcrop	-	-	-	-	yes	-	a	this study
H-14	Santa Cruz	intermed. siliceous	reworked hematite mud	outcrop	-	-	-	-	yes	-	a	this study
C-14	Santa Cruz	intermed. siliceous	chert-hematite BIF	12-24	69.9	banded	II	yes	yes	-		this study
C-15	Santa Cruz	intermed. siliceous	chert-hematite BIF	12-24	75.2	podded	I	yes	-	-		this study
C-16	Santa Cruz	transitional	chert-hematite BIF	12-24	96.24	podded	I	yes	-	-		this study
C-17	Santa Cruz	transitional	chert-hematite BIF	12-24	111.35	podded	I	yes	-	-		this study
C-01	Santa Cruz	transitional	chert-hematite BIF	24-24	142.4	banded	II	yes	-	-		this study
C-18	Santa Cruz	transitional	hematite mud	12-24	120	-	II	yes	-	-		this study
C-11	Santa Cruz	lower carbonateous	chert-dolomite-hematite BIF	24-24	215.8	weakly podded	-	-	yes	-	b	this study
C-12	Santa Cruz	lower carbonateous	dolomite-chert-hematite BIF	24-36	167.65	banded	-	-	-	yes (dol)	b	this study
C-06	Santa Cruz	lower carbonateous	dolomite-chert-hematite BIF	24-24	268.21	banded	-	-	yes	yes (dol)	c	this study
C-07	Santa Cruz	lower carbonateous	dolomite-chert-hematite BIF	24-24	268.8	weakly podded	I	yes	-	-	c	this study
C-05	Santa Cruz	lower carbonateous	dolomite-chert-hematite BIF	40-32	277.35	weakly podded	I	yes	-	-		this study
C-04	Santa Cruz	lower carbonateous	dolomite-chert-hematite BIF	40-32	278.03	banded	I	yes	-	.	d	this study
C-03	Santa Cruz	lower carbonateous	dolomite-chert-hematite BIF	40-32	290.35	banded	-	-	-	yes (dol)	d	this study

UWA ID		C-04	C-05	C-07	C-14	C-01	C-17	C-16	C-15	C-18	H-01	H-03
lithology	*detection limits*	banded dolomite-chert-hematite BIF	podded dolomite-chert-hematite BIF		banded chert-hematite BIF		podded chert-hematite BIF			hematite mud	reworked hematite mud	hematite chert
Fe		35.12	40.11	51.69	45.70	43.83	54.62	51.86	55.97	66.26	58.71	16.04
Fe2O3_t	0.01	50.21	57.35	73.90	65.34	62.67	78.09	74.14	80.02	94.74	83.94	22.94
SiO2	0.01	13.72	9.81	10.78	34.48	31.98	21.75	26.25	19.86	3.77	14.08	77.63
TiO2	0.00	0.02	0.03	0.02	0.03	0.02	0.02	0.02	0.03	0.04	0.03	0.01
Al2O3	0.01	0.08	0.25	0.07	0.14	0.07	0.09	0.09	0.16	0.19	0.14	0.06
MnO	0.00	0.18	0.55	0.08	0.11	0.21	0.07	0.05	0.11	0.09	0.01	0.01
MgO	0.01	5.05	4.78	1.53	0.03	0.63	0.03	0.01	0.03	0.09	0.03	b.d.l.
CaO	0.01	11.70	11.39	4.90	0.10	2.09	0.16	0.09	0.09	0.63	0.07	0.03
K2O	0.01	b.d.l.	0.01	b.d.l.	b.d.l.	b.d.l.	b.d.l.	b.d.l.	0.01	b.d.l.	b.d.l.	b.d.l.
Na2O	0.01	0.07	0.10	0.01	0.01	0.02	0.01	0.01	0.03	0.02	0.01	0.01
P2O5	0.01	0.36	0.37	0.38	0.14	0.20	0.15	0.10	0.10	0.39	0.11	0.02
LOI	0.01	16.99	16.20	6.54	0.28	2.76	0.37	0.20	0.35	0.51	0.32	0.14
Total	0.01	98.37	100.80	98.22	100.70	100.60	100.70	101.00	100.80	100.50	98.75	100.90
FeO*	0.10	4.00	3.50	2.00	0.50	1.60	0.90	0.70	0.30	1.00	0.40	0.60
As	0.1	4.30	5.30	4.40	5.30	7.30	4.70	5.20	4.40	10.50	5.20	3.50
Ba	1	217.00	38.00	40.00	82.00	14.00	55.00	56.00	92.00	31.00	104.00	67.00
Be	0.1	1.10	1.10	1.30	1.70	1.20	1.80	1.70	1.90	2.10	1.20	1.10
Co	0.1	2.70	4.80	1.30	2.80	2.40	1.10	1.00	1.60	4.90	0.40	0.50
Cr	0.5	8.80	10.80	14.50	9.80	10.30	13.90	12.10	14.30	15.80	15.70	23.40
Cu	0.2	3.90	3.30	2.70	8.20	8.30	3.70	5.80	4.50	8.10	8.20	38.80
Ga	0.1	b.d.l.	0.20	b.d.l.	0.30	0.30	0.30	0.20	0.20	0.30	b.d.l.	0.20
Ge	0.5	0.80	1.30	1.20	1.50	2.30	2.30	1.70	1.70	2.00	1.60	6.50
Mo	0.1	0.40	0.60	0.80	0.70	1.60	0.80	0.50	0.60	0.70	0.50	0.70
Nb	0.2	1.00	1.20	0.40	0.60	3.10	b.d.l.	b.d.l.	0.30	0.30	2.10	0.20
Ni	0.5	3.50	4.50	2.50	6.20	6.10	3.10	3.20	3.00	8.20	2.20	3.00
Pb	0.5	0.80	1.20	0.70	2.00	4.40	1.20	1.60	1.70	3.10	3.80	2.30
Rb	0.2	0.30	0.80	0.30	0.50	0.60	0.50	0.40	0.40	0.60	0.40	b.d.l.
Sr	0.2	237.00	336.00	58.40	31.90	41.00	25.30	35.60	29.00	29.40	54.60	21.00
Th	0.05	0.44	0.70	0.29	0.49	0.48	0.27	0.30	0.23	0.30	0.89	0.39
U	0.01	0.05	0.08	0.07	0.18	0.23	0.10	0.12	0.14	0.11	0.11	0.16
V	1.0	32.0	33.0	35.0	42.0	34.0	30.0	42.0	39.0	53.0	36.0	14.0
Zn	0.2	7.00	6.20	3.00	4.70	9.60	6.60	3.30	3.20	9.00	7.20	9.40
Zr	1.0	3.00	5.00	b.d.l.	8.00	7.00	3.00	5.00	12.00	4.00	3.00	34.00
Y	0.50	17.90	18.20	17.60	87.80	11.60	12.30	23.20	20.00	15.60	9.60	3.80
La	0.05	11.90	7.57	10.40	5.55	1.73	3.46	6.13	6.05	1.79	11.60	4.81
Ce	0.10	7.39	9.41	6.42	10.20	3.52	3.85	7.48	5.70	3.91	21.90	9.60
Pr	0.01	2.56	1.84	2.14	1.61	0.56	0.91	1.44	1.25	0.59	3.21	1.35
Nd	0.05	10.50	7.97	9.17	7.86	2.40	4.15	6.67	5.48	2.76	13.60	5.29
Sm	0.01	2.02	1.62	1.68	1.86	0.62	0.91	1.36	1.06	0.73	2.57	1.11
Eu	0.005	0.422	0.351	0.380	0.517	0.124	0.211	0.332	0.241	0.189	0.560	0.223
Gd	0.01	2.34	1.94	2.03	3.56	0.90	1.19	1.97	1.30	1.07	2.23	0.85
Tb	0.01	0.34	0.32	0.32	0.91	0.17	0.21	0.37	0.25	0.22	0.33	0.14
Dy	0.01	2.18	2.15	2.09	8.25	1.34	1.39	2.67	1.79	1.67	1.94	0.81
Ho	0.01	0.48	0.52	0.48	2.21	0.34	0.31	0.63	0.46	0.43	0.38	0.15
Er	0.01	1.55	1.67	1.55	7.73	1.17	0.99	2.13	1.60	1.49	1.10	0.41
Tm	0.005	0.242	0.265	0.248	1.270	0.203	0.160	0.356	0.275	0.266	0.158	0.058
Yb	0.01	1.66	1.72	1.71	9.06	1.44	1.12	2.59	2.02	1.92	1.03	0.37
Lu	0.002	0.269	0.265	0.269	1.460	0.222	0.192	0.454	0.361	0.315	0.170	0.059
REE type		I	I	II	II	I	I	I	II	III	III	
SUM_REE		43.85	37.61	38.89	62.05	14.74	19.05	34.58	27.84	17.35	60.78	25.23
SUM_LREE		34.37	28.41	29.81	27.08	8.83	13.28	23.08	19.54	9.78	52.88	22.16
SUM_HREE		9.06	8.85	8.70	34.45	5.79	5.56	11.17	8.06	7.38	7.34	2.85
La/Sm_{paas}		0.86	0.68	0.90	0.43	0.41	0.55	0.65	0.83	0.36	0.66	0.63
Pr/Sm_{paas}		0.80	0.71	0.80	0.54	0.57	0.63	0.67	0.74	0.51	0.79	0.76
Gd/Yb_{paas}		0.85	0.68	0.72	0.24	0.38	0.64	0.46	0.39	0.34	1.31	1.39
Tb/Yb_{paas}		0.75	0.68	0.68	0.37	0.43	0.68	0.52	0.45	0.42	1.17	1.38
La/Yb_{paas}		0.53	0.32	0.45	0.05	0.09	0.23	0.17	0.22	0.07	0.83	0.96
Pr/Yb_{paas}		0.49	0.34	0.40	0.06	0.12	0.26	0.18	0.20	0.10	1.00	1.17
Ce/Ce^*_{paas}		0.31	0.58	0.31	0.78	0.81	0.50	0.58	0.48	0.86	0.82	0.87
Eu/Eu^*_{paas}		0.90	0.92	0.95	0.87	0.75	0.93	0.92	0.95	0.97	1.10	1.08
Y/Ho		37.29	35.00	36.67	39.73	34.12	39.68	36.83	43.48	36.28	25.26	25.33
CaO/MgO		2.3	2.4	3.2	3.3	3.3	5.3	9.0	3.0	7.0	2.3	n.d.
Ti/Zr		18	26.1	48	39.5	11.2	14.5	43.6	52.5	25.3	21.6	4.5
TiO2/Al2O3		0.260	0.110	0.340	0.220	0.260	0.180	0.270	0.180	0.200	0.190	0.120
Cu+Pb+Zn		12	11	6	15	22	12	11	9	20	19	51
Rb/Sr		0.0013	0.0024	0.0051	0.0157	0.0146	0.0198	0.0112	0.0138	0.0204	0.0073	n.d.
Zn/Co		2.59	1.29	2.31	1.68	4	6	3.3	2	1.84	18	18.8

Locality	Sample	stratigraphic zone	lithology	n	δ57Fe*	1se	δ56Fe*,§	1se
Santa Cruz	H-15	intermediate siliceous	reworked hematite mud	3	-0.04	0.07	0.01	0.08
Santa Cruz	H-14	intermediate siliceous	reworked hematite mud	3	-0.25	0.01	-0.18	0.01
Santa Cruz	C-14	intermediate siliceous	chert-hematite BIF	3	-0.71	0.07	-0.49	0.06
Santa Cruz	C-11	lower carbonaceous	chert-dolomite-hematite BIF	3	-1.22	0.04	-0.83	0.02
Santa Cruz	C-06	lower carbonaceous	dolomite-chert-hematite BIF	3	-2.62	0.03	-1.83	0.02
Rapitan	G22.19.8	15.1m	hematitic silt	n.d.	0.944	0.023	0.635	0.013
Rapitan	G22.21.1	13.8m	hematitic jaspilite	n.d.	0.858	0.015	0.575	0.011
Rapitan	G22.21.3	13.6m	hematitic jaspilite (±calcite)	n.d.	1.196	0.045	0.821	0.039
Rapitan	G22.24.8	10.1m	hematitic jaspilite (±calcite)	n.d.	0.652	0.006	0.441	0.011
Rapitan	G22.26.1	8.8 m	hematitic mud	n.d.	-0.268	0.045	-0.182	0.011
Rapitan	G22.32.9	2 m	hematitic mud	n.d.	-0.426	0.013	-0.283	0.09
Rapitan	G22.34.7	0.2 m	hematitic silt	n.d.	-0.65	0.019	-0.431	0.016

locality	stratigraphic zone	lithology	mineral	sample ID	mineral sample ID	d^{13}C VPDB	data source
Santa Cruz	lower carbonaceous	dolomite-chert-hematite BIF	dolomite-cryptocrystalline hematite band	C-03	3C carb1	-3.8	present study
				C-03	3C carb1-re	-3.8	present study (repeat)
				C-03	3C carb2	-3.7	present study
				C-03	3C carb2-re	-3.7	present study (repeat)
	intermediate carbonaceous			C-06	6C carb1	-4.3	present study
				C-06	6C carb1-re	-4.1	present study (repeat)
				C-06	6C carb2	-4.0	present study
				C-06	6C carb2-re	-4.0	present study (repeat)
	intermediate carbonaceous			C-12	12C carb1	-3.4	present study
				C-12	12C carb1-re	-3.5	present study (repeat)
				C-12	12C carb2	-3.4	present study
				C-12	12C carb2-re	-3.5	present study (repeat)
Urucum		chert-dolomite-hematite BIF	dolomite-cryptocrystalline hematite band		U-2-6	-7.02	Klein and Ladeira 2004
					U-2-1	-6.09	
					U-2-3	-5.83	
					U-2-7	-4.88	
					U-2-8	-4.49	
					U-2-9	-4.42	
Rapitan		nodular IF banded IF IF arenite	calcite		Y-7_142 Y-7_152.8 Y-5_158.7	-3.37 -2.74 -0.67	Klein and Beukes 1993

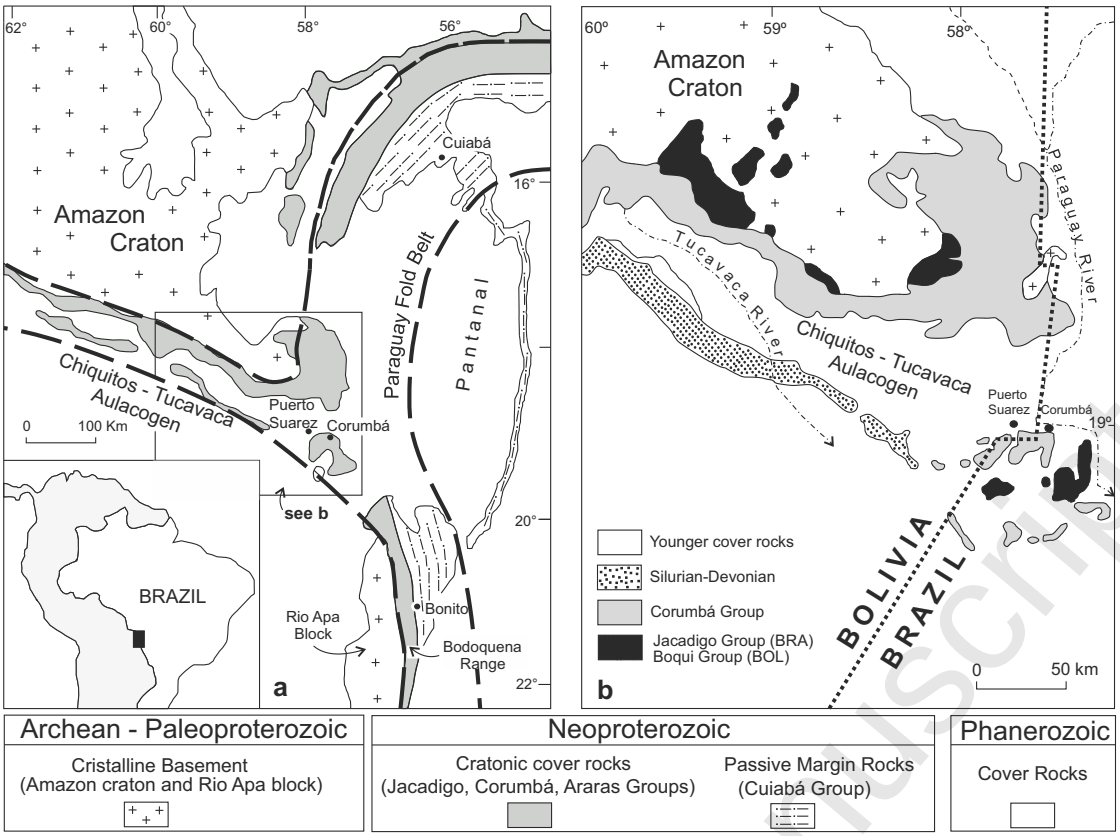

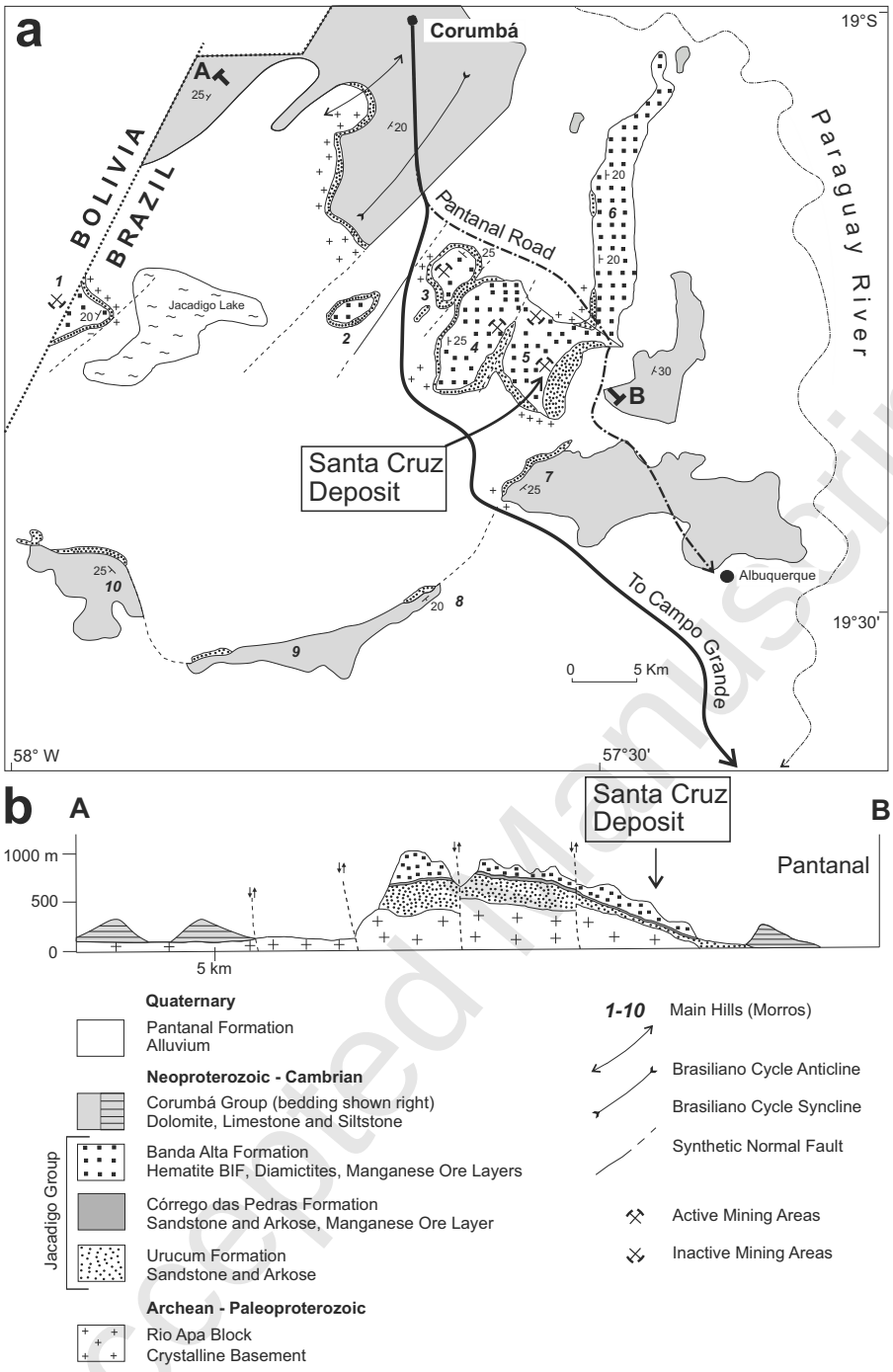

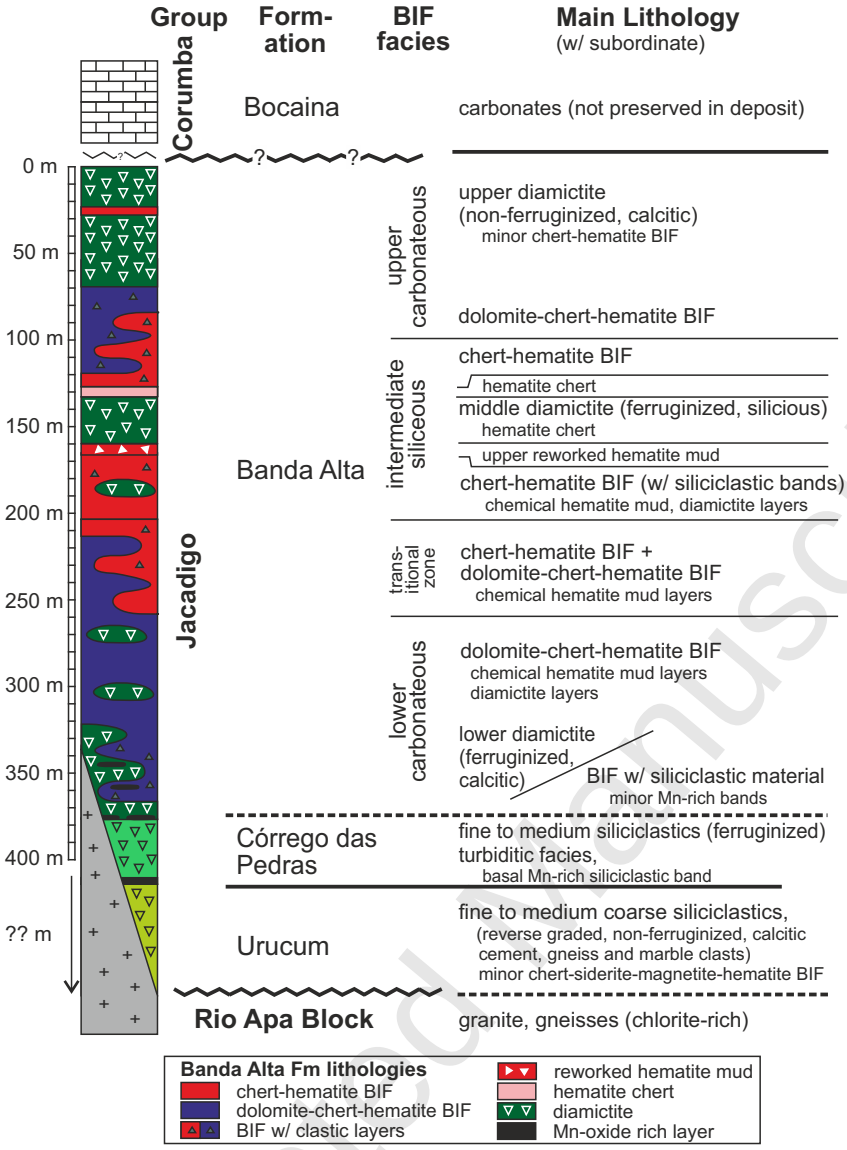

a) NW-SE-SSE cross section

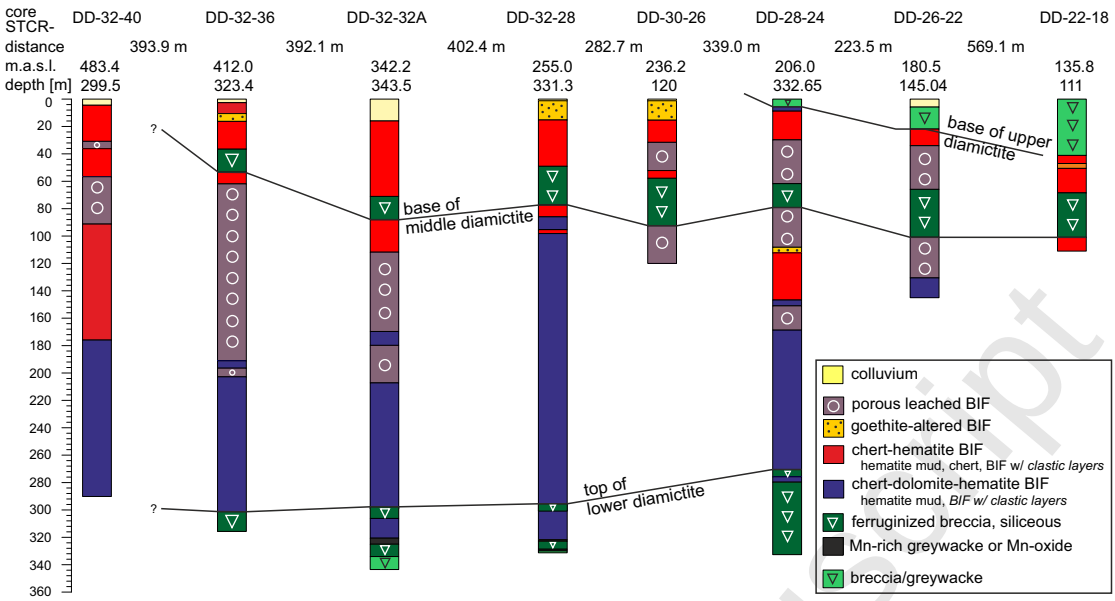

b) SSW-NNE cross section

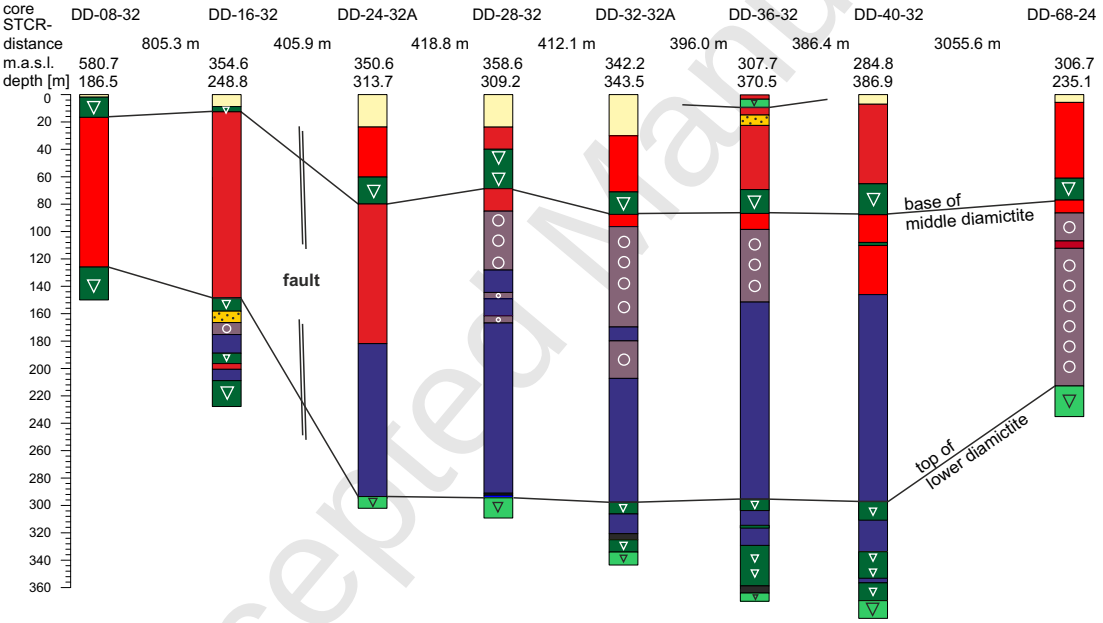

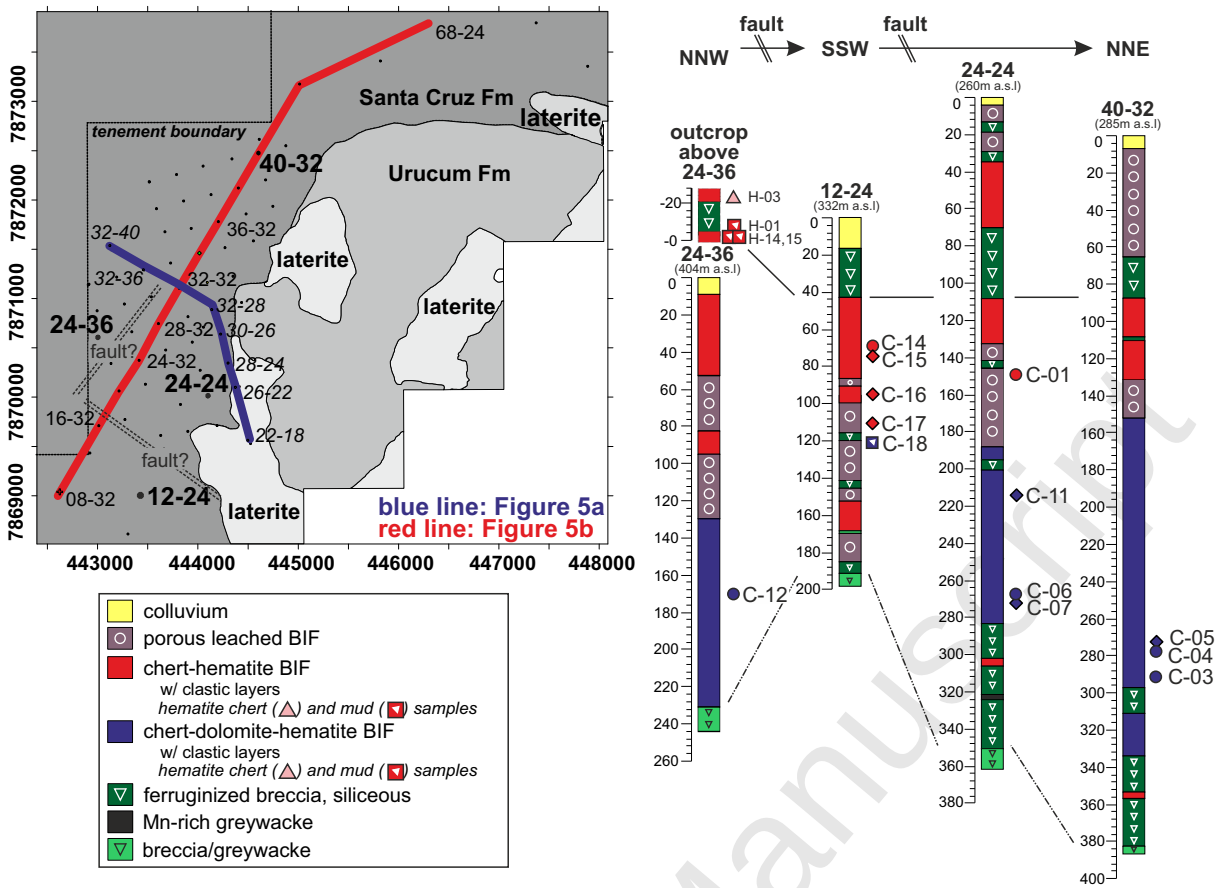

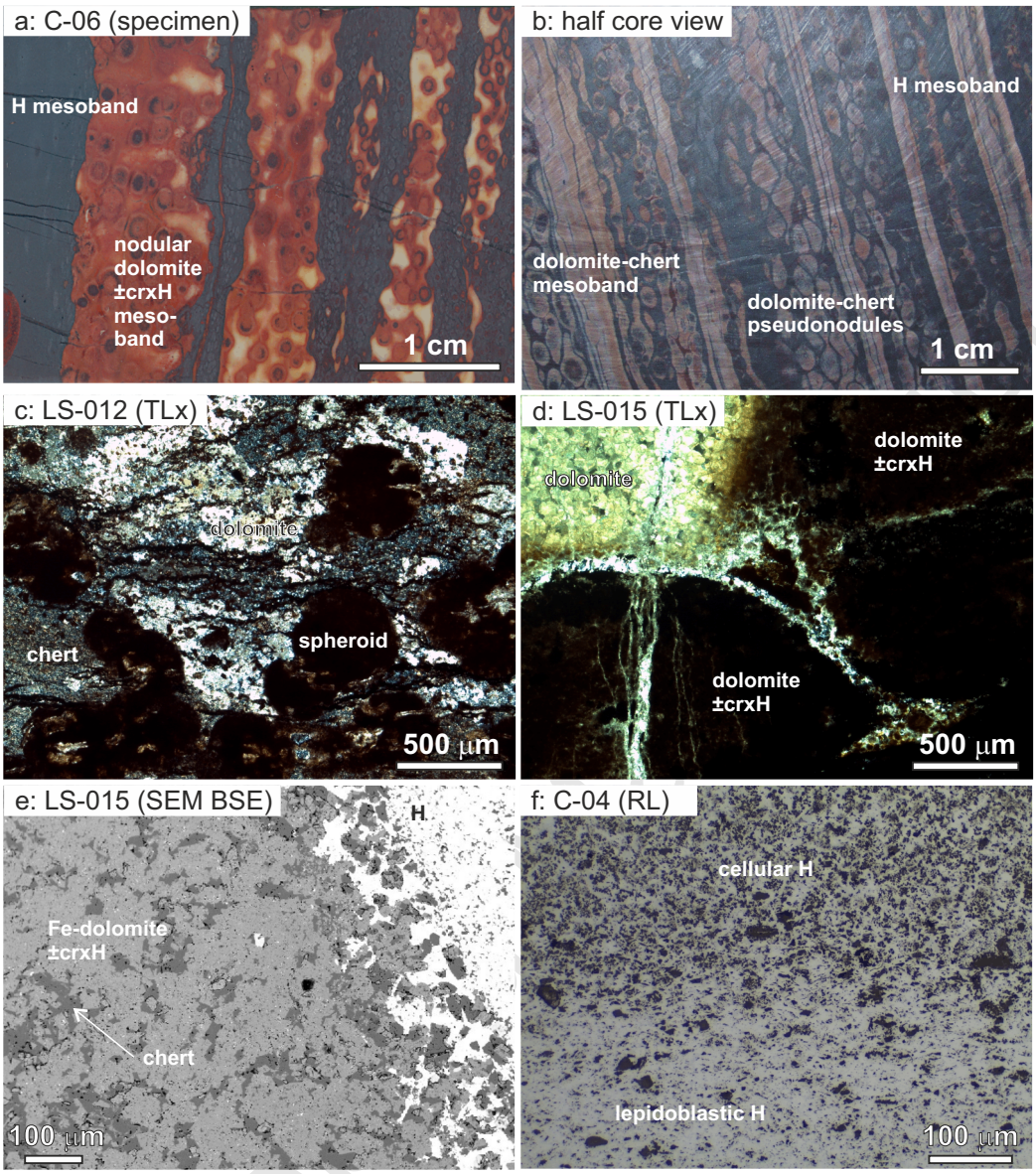

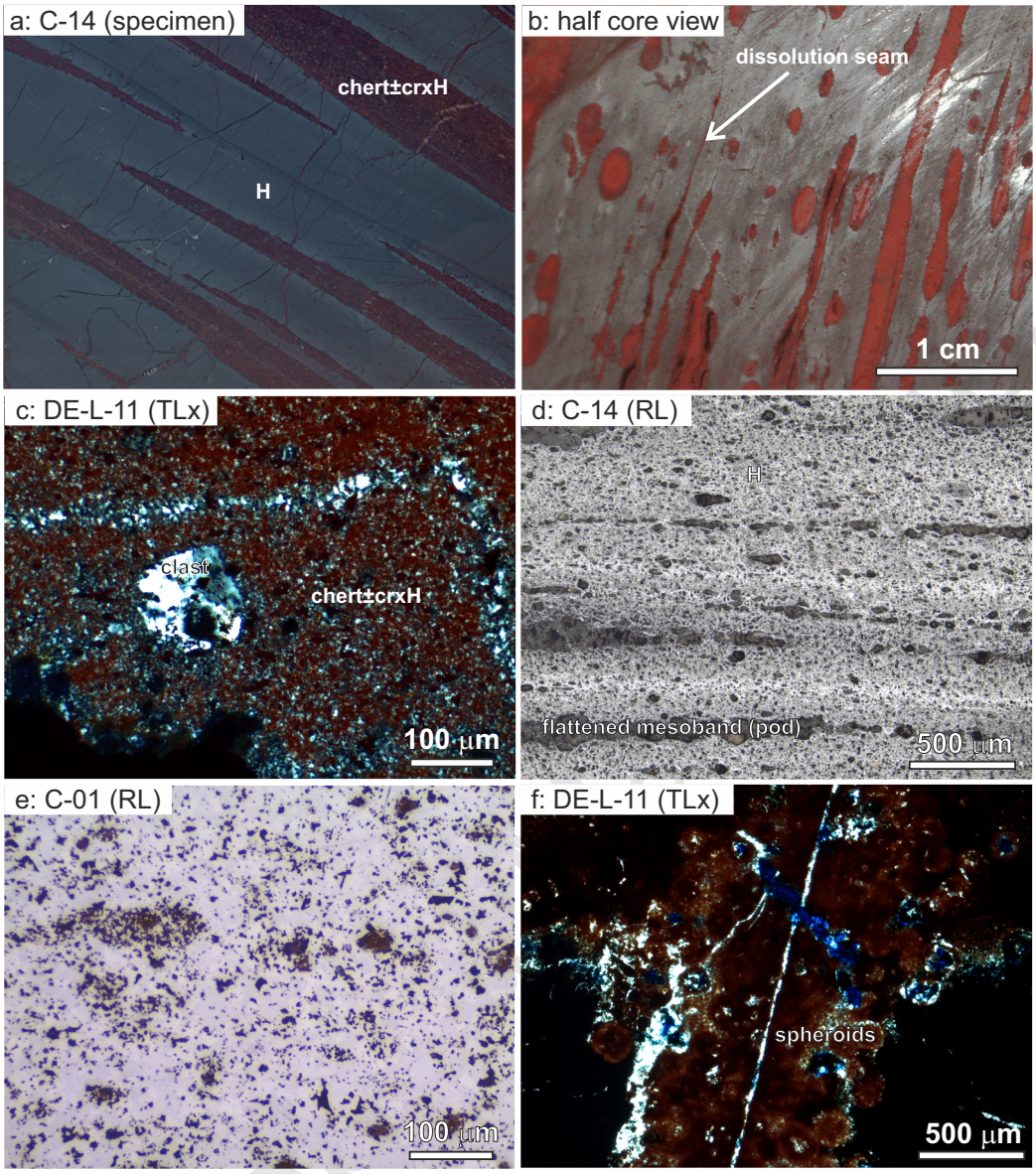

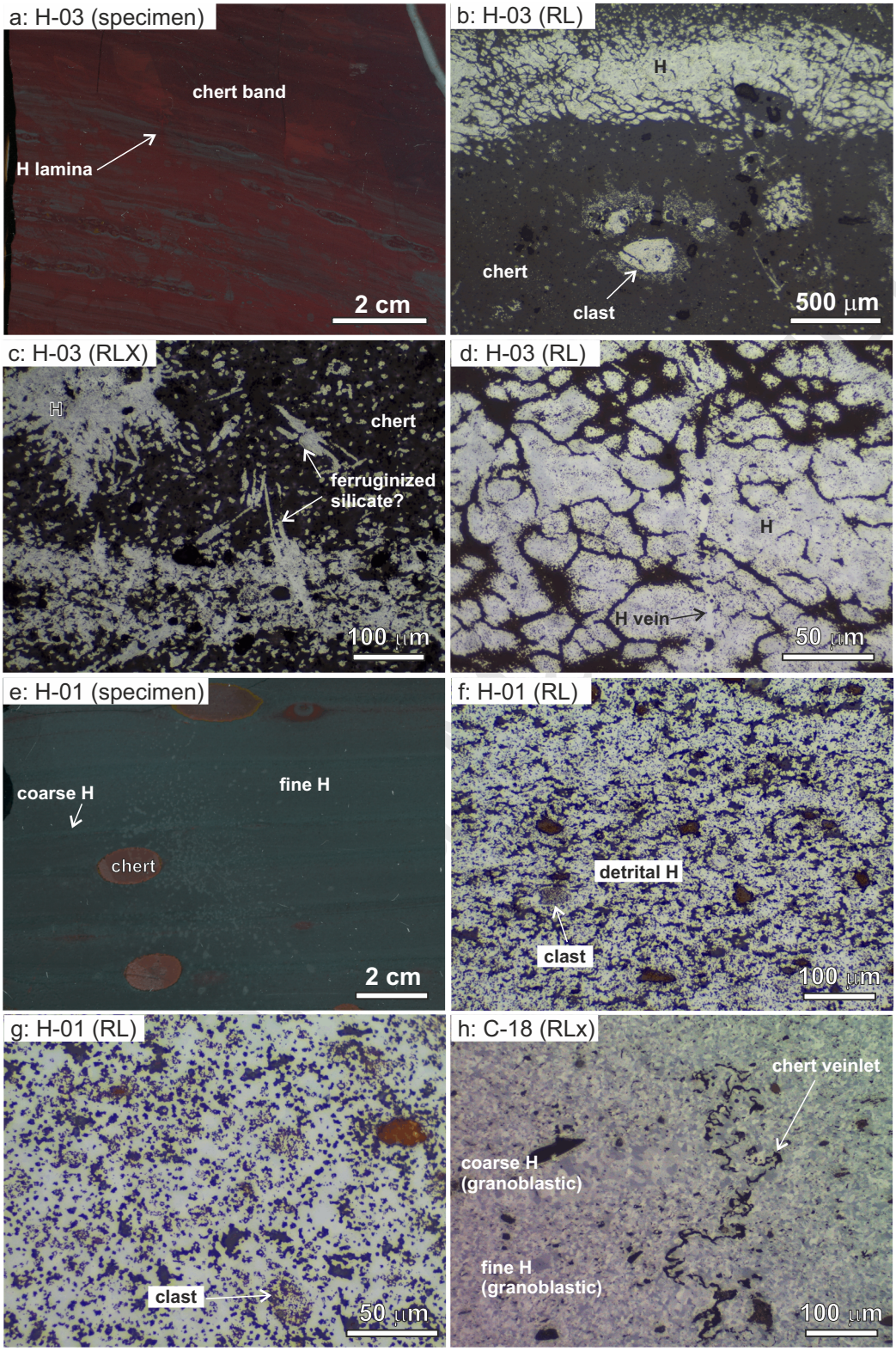

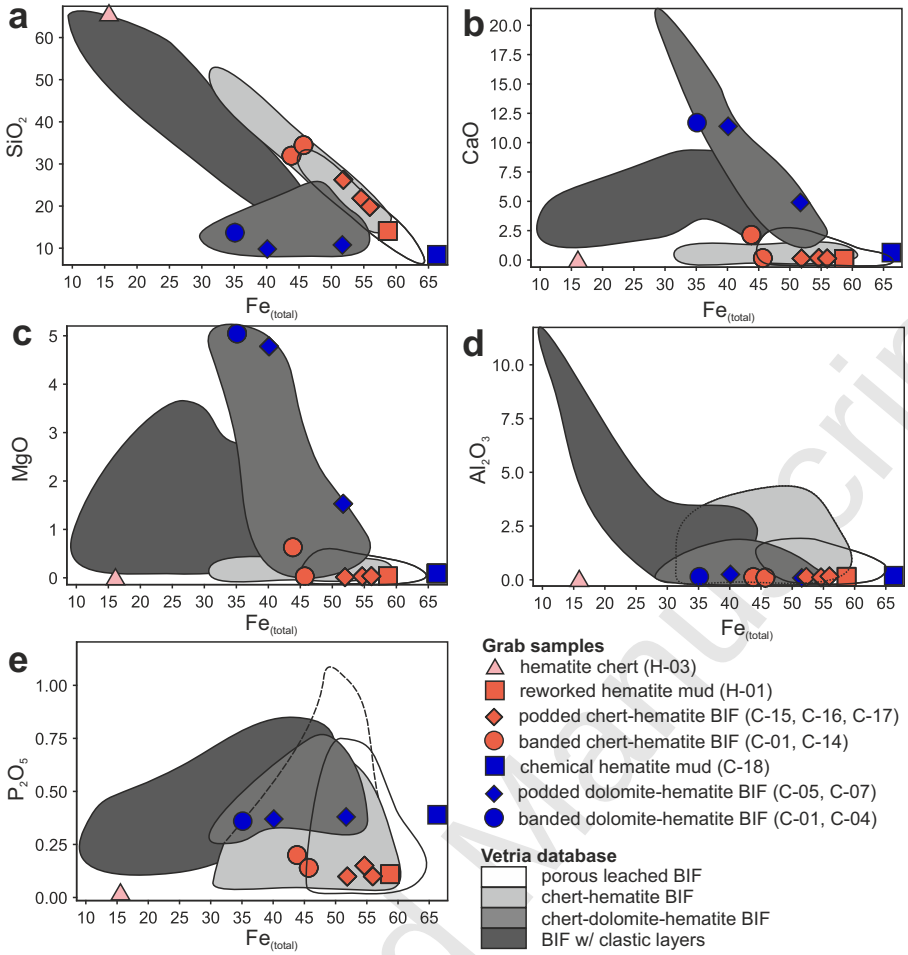

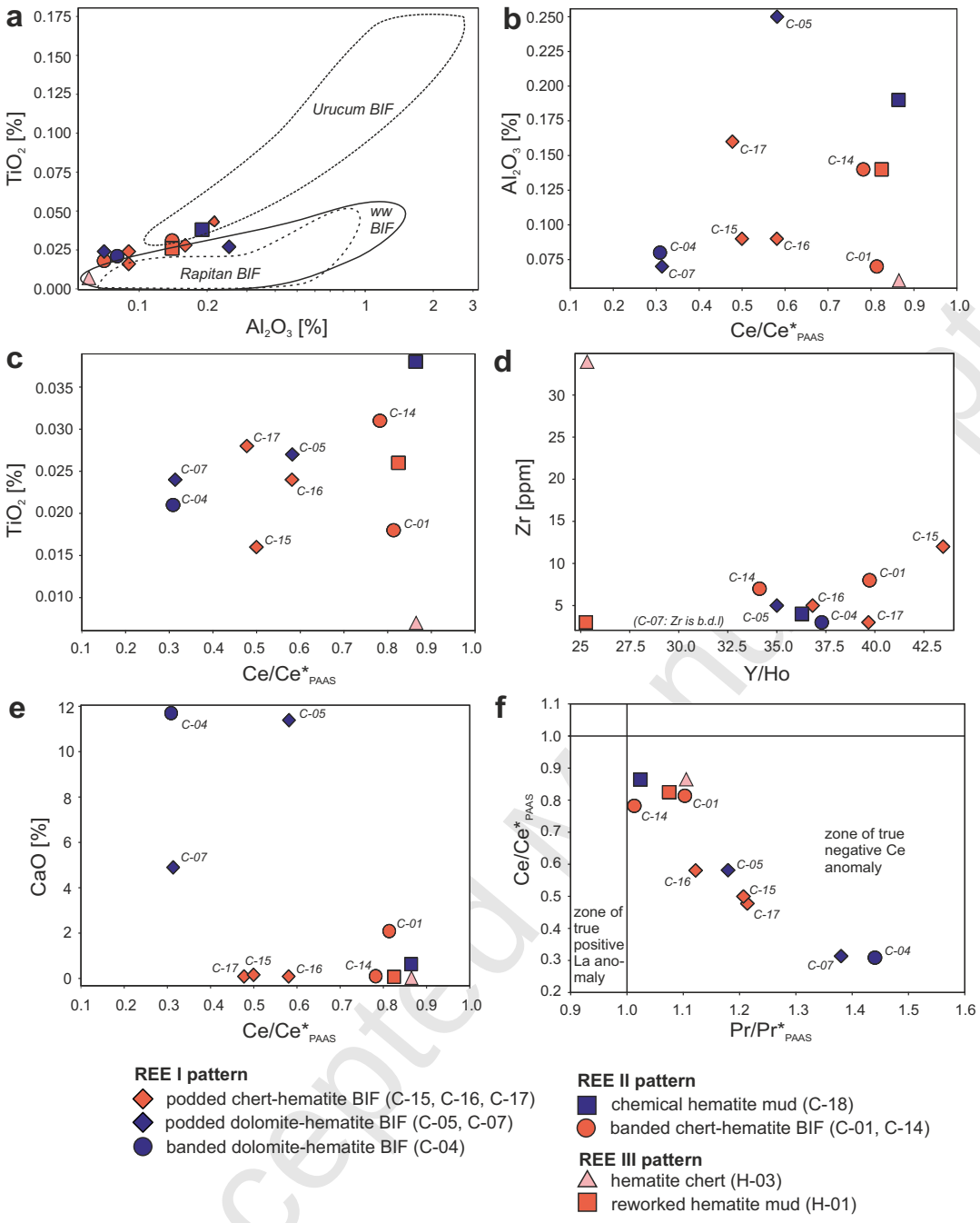

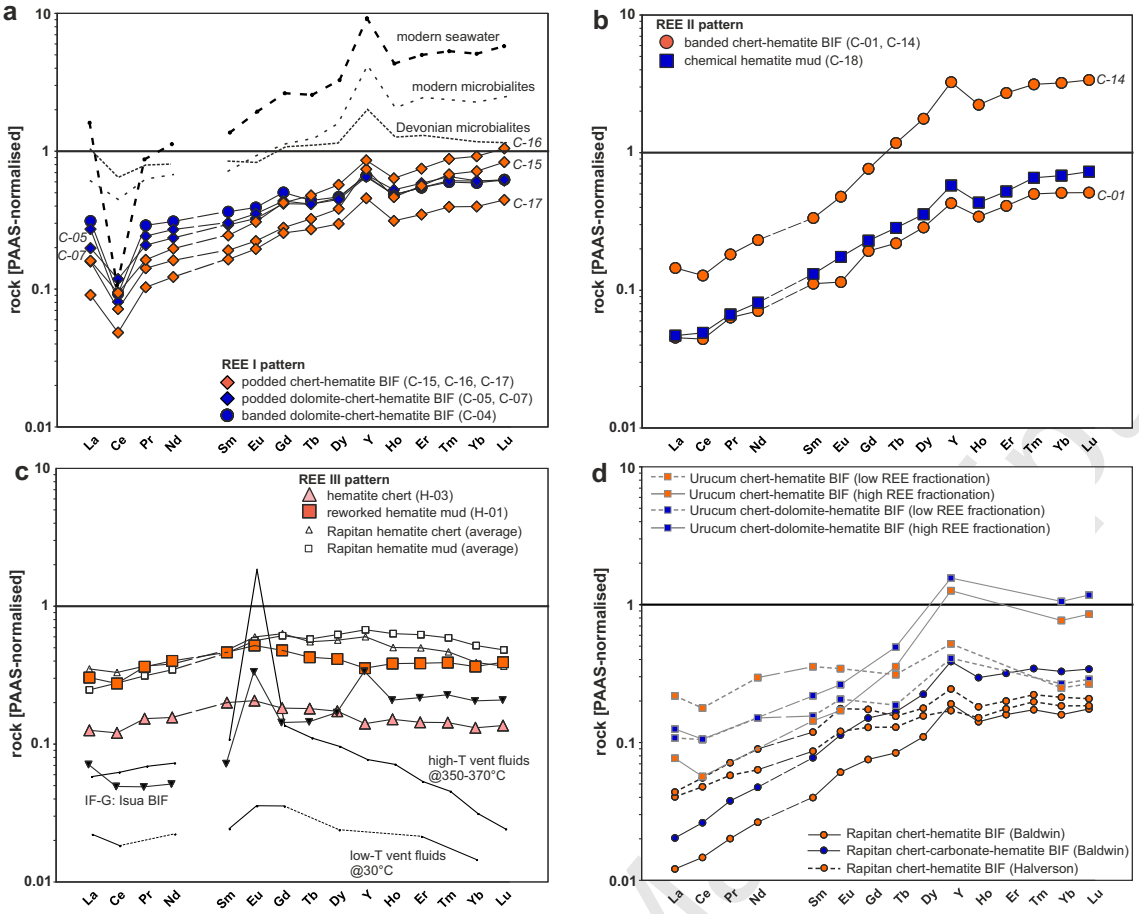

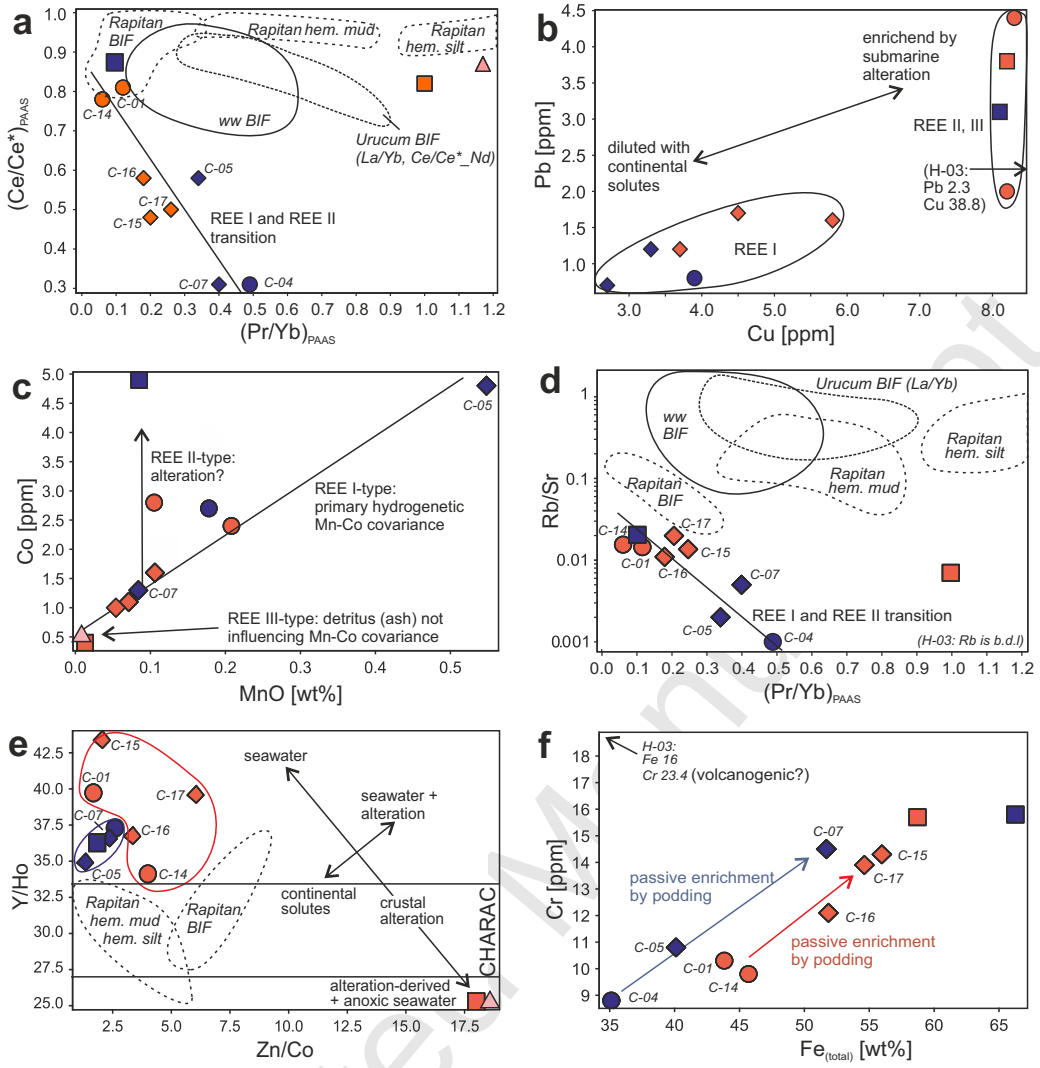

REE I pattern
- podded chert-hematite BIF (C-15, C-16, C-17)
- podded dolomite-hematite BIF (C-05, C-07)
- banded dolomite-hematite BIF (C-04)

REE II pattern
- chemical hematite "mud" (C-18)
- banded chert-hematite BIF (C-01, C-14)

REE III pattern
- hematite chert (H-03)
- reworked hematite "mud" (H-01)